A Microphysics-Scheme-Consistent Snow Optical Parameterization for the Community Radiative Transfer Model

TONG REN,[a] PING YANG,[a,b,c] KEVIN GARRETT,[d] YINGTAO MA,[d,e] JIACHEN DING,[a] AND JAMES COY[a]

[a] *Department of Atmospheric Sciences, Texas A&M University, College Station, Texas*
[b] *Department of Oceanography, Texas A&M University, College Station, Texas*
[c] *Department of Physics and Astronomy, Texas A&M University, College Station, Texas*
[d] *NOAA/NESDIS/Center for Satellite Applications and Research, College Park, Maryland*
[e] *Cooperative Institute for Research in the Atmosphere, Colorado State University, Fort Collins, Colorado*

(Manuscript received 19 May 2022, in final form 8 October 2022)

ABSTRACT: The satellite observational data assimilation community requires consistent hydrometer descriptions—including mass–size relation and particle size distribution—to be used in both the forecast model and observation operator. We develop a microphysics-scheme-consistent snow and graupel single-scattering property database to meet this requirement. In this database, snowflakes are modeled as a mixture of small column and large aggregated ice particles, the mixing ratios of which may be adjusted to satisfy a given mass–size relation. Snow single-scattering properties are computed for four different mass–size relations. Subsequently, the snow description in the Thompson microphysics scheme is used as an example to demonstrate how microphysics-scheme-consistent snow bulk optical properties are derived. The Thompson-scheme-consistent snow bulk optical properties are added to the Community Radiative Transfer Model (CRTM), version 2.4.0. With *CloudSat* Cloud Profiling Radar (CPR) snow and liquid precipitation retrievals as the inputs, CRTM simulations are performed over global oceans and compared with four collocated Global Precipitation Measurement (GPM) Microwave Imager (GMI) high-frequency channel observations. The CRTM simulated brightness temperatures show agreement with the GMI observed brightness temperatures in cases of light-to-moderate precipitation over extratropical and polar ice-free oceans, with root-mean-square errors of 4.3, 13.0, 1.8, and 3.3 K in the 166-GHz (vertical polarization), 166-GHz (horizontal polarization), 183 ± 3-GHz (vertical polarization), and 183 ± 7-GHz (vertical polarization) channels, respectively. The result demonstrates the potential of using the newly developed microphysics-scheme-consistent snow optical parameterization in data assimilation applications.

KEYWORDS: Atmosphere; Databases; Microwave observations; Radars/radar observations; Satellite observations; Data assimilation

1. Introduction

Satellite observations are often used to evaluate large-scale and regional model simulations (e.g., Dolinar et al. 2015; Huang et al. 2014; Jiang et al. 2012; Masunaga et al. 2008; Qu et al. 2018; Su et al. 2013; Vignesh et al. 2020; Zhou et al. 2007). Microwave (MW) radars and radiometers can detect large hydrometers in the atmosphere, and hence are used to examine model cloud and precipitation simulations. Zhou et al. (2007) compared Tropical Rainfall Measuring Mission (TRMM; Kummerow et al. 2000) Microwave Imager (TMI) and Precipitation Radar (PR) (Kummerow et al. 1998) hydrometer profile measurements during the South China Sea Monsoon Experiment (SCSMEX) field campaign with Goddard Cumulus Ensemble (GCE) model simulations. Masunaga et al. (2008) compared TRMM PR and *CloudSat* (Stephens et al. 2002) Cloud Profiling Radar (CPR; Tanelli et al. 2008) measurements with a global cloud-resolving model simulation of a Madden–Julian oscillation (MJO; Madden and Julian 1971, 1972) event. Eliasson et al. (2011) compared the National Environmental Satellite Data and Information Service (NESDIS) Microwave Surface and Precipitation Products System (MSPPS) and *CloudSat* CPR monthly mean ice water path (IWP) retrievals (Austin et al. 2009; Ferraro et al. 2005) with climate model simulations. In addition to comparisons of MW cloud and precipitation retrievals and model simulations, model simulated atmospheric states are linked to spaceborne MW sensor radiance measurements through radiative transfer calculations (e.g., Masunaga et al. 2010; Matsui et al. 2013). The Goddard profiling algorithm (GPROF; Kummerow et al. 1996, 2001) linked simulated vertical distributions of hydrometeors to satellite MW brightness temperature (BT) measurements. Based on the Goddard Satellite Data Simulation Unit (SDSU; Matsui et al. 2009, 2013), radiance measurements from different spaceborne instruments can be directly used to evaluate regional Earth system model simulations (Matsui et al. 2014). With the simulated atmospheric state of a heavy-snow event over France based on a mesoscale cloud model, Galligani et al. (2015) computed MW BTs using the Atmospheric Radiative Transfer Simulator (ARTS; Eriksson et al. 2011) and compared the results with Microwave Humidity Sounder (MHS) measurements.

Several weather forecasting centers have operationally assimilated satellite radiance measurements in all-sky conditions (Bauer et al. 2010, 2011; Geer et al. 2010, 2017, 2018; Zhu et al. 2016). The Radiative Transfer Model (RTM) for Television Infrared Observation Satellite (TIROS) Operational Vertical Sounder (RTTOV; Saunders et al. 2018) and the Community Radiative Transfer Model (CRTM; Han et al. 2006)

Corresponding author: Tong Ren, tr7585@tamu.edu

DOI: 10.1175/MWR-D-22-0145.1

TABLE 1. Example databases of nonspherical ice particle single-scattering properties frequently used in snow or graupel studies.

Database	Particle shape	Frequencies	Temperature
Matrosov (2007)	Oblate spheroids resembling aggregates and single dendrite crystals	Ka (34.6 GHz) and W (94 GHz) bands	−5°C
Hong (2007a,b)	Column, hollow, plate, 6-branch bullet rosette, aggregate of columns, and droxtal	5 frequencies from 89 to 340 GHz	−30°C
Liu (2008b)	Columns, plates, bullet-rosettes, sectors, and dendrites	10 frequencies from 13.4 to 340 GHz	−40°, −30°, −20°, −10°, and 0°C
Kuo et al. (2016)	Dendrites, needles, plates, and their aggregates	Global Precipitation Measurement mission (GPM; Hou et al. 2014) Microwave Imager (GMI) and dual-frequency precipitation radar (DPR) frequencies	Unknown
Lu et al. (2016)	Aggregates, branched planar crystals, plates, columns, and conical graupel	X (9.4 GHz), Ku (13.4 GHz), Ka (35.7 GHz), and W (94 GHz) bands	0°C
Ding et al. (2017b)	10-plate aggregate, 5-plate aggregate, 8-column aggregate, solid hexagonal column, hollow hexagonal column, hexagonal plate, solid bullet rosette, hollow bullet rosette, droxtal, oblate spheroid, and prolate spheroid	41 frequencies from 1 to 874 GHz	160, 200, 230, and 270 K
Eriksson et al. (2018)	16 single cystal shapes, including plates, columns, Icosahedral nonhydrostatic GCM (ICON) cloud ice, Global Environmental Multiscale Model (GEM) cloud ice, bullet rosettes, and sector; 13 aggregate shapes, including Evans et al. (2012) snow, Tyynelä et al. (2011) dendrite, column, block, and plate aggregates, ICON and GEM hail, snow, and graupel, and spherical graupel	34 frequencies from 1 to 886.4 GHz	190, 230, and 270 K

are two RTMs adopted by weather forecasting centers for data assimilation applications. Both models have been extensively used to simulate satellite infrared (IR) and MW signals (e.g., Greenwald et al. 2016; Lu et al. 2020; Otkin et al. 2009). Previous studies made efforts to improve the two RTMs, such as improving cloud overlap treatment (Geer et al. 2009) and representation of frozen hydrometeor optical properties (Geer and Baordo 2014; Yi et al. 2016). However, Geer et al. (2018) identified three issues in representing clouds and precipitation in all-sky satellite data assimilation. First, hydrometeor variables are not always available to the radiative transfer operator. In addition, inconsistent assumptions (e.g., particle size distributions) are often made in the forecast model and in the radiative transfer operator. Moreover, important cloud and precipitation representation details (e.g., particle orientation) needed in radiative transfer computations remain poorly known, and for example not predicted by models. Furthermore, it is sometimes unclear how the parameterized hydrometer bulk optical properties are computed in a radiative transfer operator; for instance, no document has been archived as to the computational details of frozen hydrometer bulk optical properties in the CRTM (Sieron et al. 2017; Stegmann et al. 2018).

Previous studies pointed out the drawbacks of modeling frozen hydrometeors as spheres in computing their optical properties in the MW region (e.g., Kim et al. 2007; Kulie et al. 2010; Leinonen et al. 2012; Matrosov 2007). Geer and Baordo (2014) suggested that spherical frozen hydrometers produce overly high scattering in 30–50 GHz and overly low scattering in 150–183 GHz. Since the inadequacy of the spherical model was realized and more computational resources became available, computations of frozen hydrometer single-scattering properties have focused on nonspherical particles (Kim 2006; Liu 2004; Petty and Huang 2010) and databases of a variety of nonspherical ice particle shapes have been developed. Table 1 documents some databases that are frequently applied in snow or graupel studies. More comprehensive surveys of the databases can be found in Eriksson et al. (2018) and Tyynelä and von Lerber (2019). The database of Liu (2008b) in Table 1 was later extended to include an aggregate of 6-branch bullet-rosettes (Honeyager et al. 2016; Nowell et al. 2013). The single-scattering properties of the 6-branch bullet-rosette (6BR) and dendrite in Liu (2008b) were used to simulate MW radiometer signals for snowfall events (Skofronick-Jackson and Johnson 2011). The databases of Matrosov (2007), Liu (2008b), and Hong (2007a,b) have been used in ground-based and spaceborne millimeter-wavelength radar snow retrievals (Kulie et al. 2010; Liu 2008a; Matrosov and Battaglia 2009; Matrosov et al. 2008). The database of Hong (2007a,b) was later extended to more frequencies between 100 and 1000 GHz (Hong et al. 2009b) and compared with the Liu (2008b) database in Eriksson et al. (2015). The scattering properties of frozen aggregate particles in Kuo et al. (2016) have been tested using aircraft measurements (Olson et al. 2016) and applied in

the Global Precipitation Measurement (GPM) Dual-Frequency Precipitation Radar (DPR) snow retrievals (Chase et al. 2021). With the aggregate particle radiative properties at submillimeter and millimeter wavelengths (Ding et al. 2017b) and infrared (IR) wavelengths (Yang et al. 2013), Coy et al. (2020) studied the possibility of retrieving cirrus ice water content and mean particle size using both spaceborne submillimeter/millimeter and IR instruments. Different frozen hydrometeor models in the database of Eriksson et al. (2018) were tested with aircraft and satellite passive and active observations (Ekelund et al. 2020; Fox 2020; Fox et al. 2019). Based on the Liu (2008b) and Eriksson et al. (2018) databases, hydrometeor bulk optical properties have been derived for the RTTOV applications (Geer 2021; Geer et al. 2021).

Previous studies suggested that consistent ice optical model and size distributions be used in microphysics and radiation parameterization schemes (Baran 2012; Baran et al. 2014; Thompson et al. 2016). With the focus of the data assimilation community turning to all-sky data assimilation, it becomes important to develop microphysics-scheme consistent frozen hydrometeor bulk optical parameterizations (e.g., Sieron et al. 2017, 2018). With the particle size distribution from cloud microphysics schemes, Sieron et al. (2018) replaced the CRTM snow optical parameterization by the bulk optical properties of nonspherical particles in Liu (2008b) and compared BT simulations with satellite observations during the rapid intensification stage of a destructive hurricane. With the microphysics-scheme consistent snow optical parameterization added to CRTM (Liu 2008b), Zhang et al. (2021) showed improved forecasts of the track, intensity, and rainfall of Hurricane Harvey (2017) via assimilating all-sky MW radiances. As stated in Sieron et al. (2017), the motivation of developing microphysics-scheme consistent hydrometer optical parameterizations is to facilitate a more meaningful constraint of spaceborne radiometric observations on the simulated atmospheric state. Inspired by these recent studies, through the design of snow and graupel shapes, we develop new microphysics-scheme consistent snow and graupel optical models for data assimilation and remote sensing applications. Section 2 describes the snow and graupel models and the incorporation of the snow bulk optical parameterization into the CRTM. Section 3 introduces the data and methods used to test the snow parameterization. The test results are presented in section 4, followed by conclusions in section 5.

2. Snow and graupel optical models

Many all-sky radiative transfer simulation studies have achieved the consistency between single-scattering and microphysical properties with different approaches. Some individual snow shapes in the ARTS database (Eriksson et al. 2018) are specifically designed to have properties that are consistent with certain microphysics schemes. Previous studies have suggested different strategies of computing snow bulk optical properties, if a snow mass (m)–size (or maximum dimension, D) relation of interest cannot be represented by any snow shape in existing databases. Geer and Baordo (2014) calculate snow bulk optical properties using a snow particle size distribution whose free parameter is adjusted to match a given snow water content (SWC). Sieron et al. (2018) calculate snow bulk optical properties using a snow particle size distribution adjusted to preserve a given snow particle mass distribution. Ori et al. (2021) simulate W-band radar reflectivity with the Liu (2008b) backscattering cross sections of individual snow particles of size D being scaled by the ratio of a given squared mass to that in the Liu (2008b) database.

Vapor deposition and aggregation are the two main mechanisms of snow growth (Matrosov and Battaglia 2009). Previous studies recommended that a mixture of small pristine ice particles and large snow aggregates be adopted for more realistic snow radiative scattering calculations (e.g., Kneifel et al. 2011). The mixture of two habits was assumed in the development of a cloud ice optical model that best fits aircraft ice water content measurements (Liu et al. 2014; Loeb et al. 2018), and the cloud ice model also showed best agreement with the Thompson microphysics scheme (Thompson and Eidhammer 2014; Thompson et al. 2004, 2008) m–D relation (Ren et al. 2021). Based on the previous mixture model recommendation, in our snow model, snowflake particles are designed to be a mixture of surface-roughened hexagon columns with aspect ratio 1 and dendrite aggregates (Fig. 1a). The dendrite aggregate is generated by randomly attaching 20 dendrites with varying sizes and height–diameter ratios. The diameter D_d of each of the 20 dendrites is arbitrarily specified between 0.05 and 0.35 cm. The height H_d of each dendrite is determined from the relation $H_d = 9.96 \times 10^{-3} D_d^{0.415}$ (Pruppacher and Klett 2010). Then, the dendrite aggregate dimension is uniformly scaled to the simulated sizes, resulting in an m–D relation of $m = 4.537D^3$, where m is in kilograms and D is in meters. Both columns and aggregates are assumed to be randomly oriented with an equal number of mirror-imaging orientations. Under this orientation condition, the scattering phase matrix has six independent nonzero elements (van de Hulst 1957). While particle orientations are not of interest in some cloud microphysics schemes, satellite polarimetric signals over ice cloud scenes are sensitive to ice particle orientations (e.g., Barlakas et al. 2021; Brath et al. 2020; Gong and Wu 2017). Because our snow model assumes randomly oriented particles, the impact of ice particle orientations on snow polarimetric properties is not considered in our model. The height of the column and the diameter of the circumscribed sphere of the aggregate are taken as the maximum dimensions of the two habits. The mixing ratios of columns and aggregates can be adjusted to fit the mixture of the two habits to m–D relations in microphysics schemes in a size range.

Let $N(D)$ be a snow particle size number distribution. The $N(D)$ represents the total number of particles per unit volume in the size interval between D and $D + dD$, where the total number means the sum of the number of column particles and the number of dendrite aggregate particles. Let $f_1(D)$ and $1 - f_1(D)$ be the number concentration mixing ratios of the columns and dendrite aggregates, respectively; then $N(D)f_1(D)$ and $N(D)[1 - f_1(D)]$ represent the particle size distributions of the two individual habits. Given an m–D relation $m = h(D)$ of interest, the mixing ratio $f_1(\mathrm{D})$ can be adjusted to make the mixture of the two habits have the m–D relation in a size range. Let $m_1(D)$ and $m_2(D)$ be the

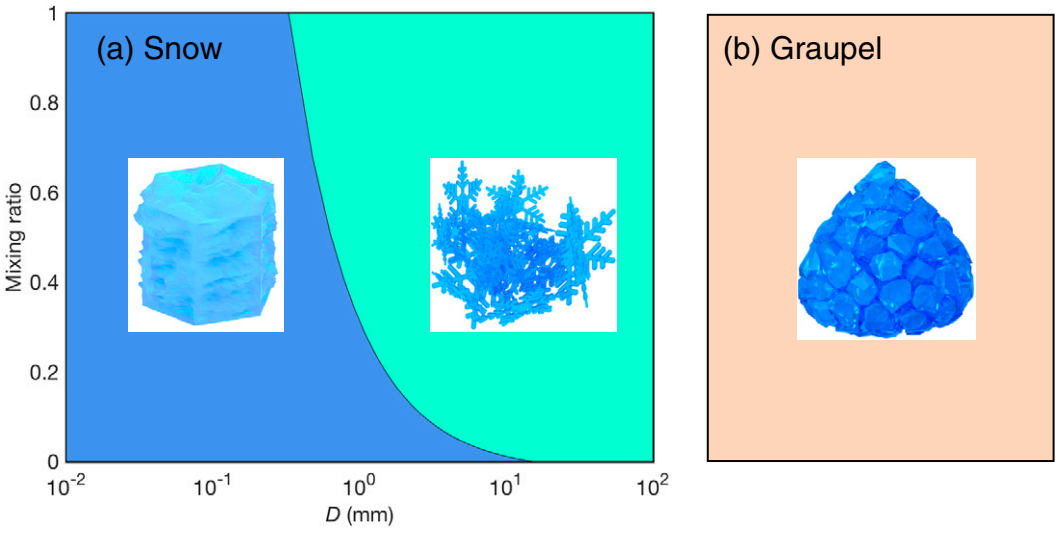

FIG. 1. The modeled shapes of (a) snow and (b) graupel.

masses of the two habits of size D. We seek a mixing ratio $f_1(D)$ such that

$$f_1(D)m_1(D) + [1 - f_1(D)]m_2(D) = h(D). \quad (1)$$

However, solving $f_1(D)$ with Eq. (1) always results in $f_1(D) > 1$ in some size interval $D \le D_1$ and $f_1(D) < 0$ in some size interval $D \ge D_2$. To avoid an unrealistic solution for $f_1(D)$, we set $f_1(D) = 1$ when $f_1(D) > 1$ and $f_1(D) = 0$ when $f_1(D) < 0$. For example, the following snow m–D relation of Cox (1988) is used in the Thompson microphysics scheme:

$$m = 0.069D^2, \quad (2)$$

where m is in kilograms and D is in meters. With a mixture of the columns and aggregates illustrated in Fig. 1a, snowflakes have the m–D relation in Eq. (2) in the size range $0.3 < D < 15.2$ mm. Snow particles are only columns when $D \le 0.3$ mm and only aggregates when $D \ge 15.2$ mm. In the size interval $D_1 < D < D_2$, snow particles consist of both columns and aggregates; assuming that snow particles are independent scatterers, we calculate the mean single-scattering properties—including ice portion volume $V(D)$, projected area averaged over all particle random orientations $A(D)$, extinction efficiency $Q_{\text{ext}}(D)$, single-scattering albedo $\omega'(D)$, asymmetry factor $g'(D)$, and scattering phase function $p'(D)$—by averaging the properties of the two habits with the weights of $f_1(D)$ and $1 - f_1(D)$. Note that any property that is not a linear combination of the property of individual ice particles—such as aggregation, riming rate, and fall speed—cannot be properly described by a mixture model, although a mixture snow model can be adjusted to achieve a given m–D relation. Some snow habits in the ARTS database are specifically designed to be consistent with certain microphysics schemes to overcome the problem. It should also be noted that if a microphysics scheme strictly requires that the assumed m–D relation applies to every single particle, then a mixture model should not be used (Sieron et al. 2017, 2018).

For the graupel model presented here, particles are assumed to be randomly oriented cones (Fig. 1b), the mathematical description of which is given by Wang (1982).

In this work, a synergistic combination (Yang et al. 2019) of the Invariant Imbedding **T**-Matrix (II-TM) method (Bi and Yang 2014; Johnson 1988) and the Improved Geometric Optics Method (IGOM; Yang and Liou 1996) are used to compute the snow and graupel single-scattering properties from the ultraviolet (UV) to IR regions with the ice refractive index at 266 K (Warren and Brandt 2008) and MW region with the ice refractive indices at 5 different temperatures (Iwabuchi and Yang 2011). Table 2 documents the dimensions of the snow and graupel single-scattering property database. The UV-to-IR region includes 470 wavelengths from 0.2 to 200 μm. There are 70 frequencies available in the MW region in our snow and graupel database.[1] The II-TM method and IGOM apply to small and large size parameters, respectively. The radiative properties of graupel are sensitive to its bulk density (Tang et al. 2017), and hence single-scattering computations are performed for graupel particles that have different values of mass ratio defined as the ratio of the mass density of a graupel particle to that of solid ice. This study focuses on testing the microphysics-scheme consistent snow bulk optical parameterization.

Passive and active observables are sensitive to the size measure of solid hydrometeor particles (Johnson et al. 2012). The bulk optical properties—including the mass extinction coefficient $\beta_{\text{ext},m}$, single-scattering albedo ω, asymmetry factor g, and phase function p—can be parameterized in terms of SWC and a certain measure of the mean size of snowflakes. The effective radius (r_{eff}; Foot 1988) in Eq. (3) is an optimal mean

[1] 1, 1.4, 3, 5, 6.8, 6.925, 9, 10, 10.7, 13.4, 15, 18.7, 19, 19.35, 21.3, 22.234, 23.8, 24.1, 31.4, 35.6, 36.5, 37, 50, 50.3, 52.8, 53.506, 54.4, 54.94, 55.5, 57.29, 59.4, 60.0, 60.672, 63.283, 70, 75, 80, 85.5, 89, 90, 91.655, 94, 114.5, 115.95, 116.65, 117.8, 118, 150, 157, 166, 183.31, 190.31, 205, 220, 240, 243, 325, 325.15, 340, 380, 425, 448, 462, 487, 500, 640, 643, 664, 683, and 874 GHz.

TABLE 2. Dimensions of the snow and graupel single-scattering database in this study.

	Snow		Graupel	
Spectral range	UV-IR (0.2–200 μm)	MW (1–874 GHz)	UV-IR (0.2–200 μm)	MW (1–874 GHz)
Spectral resolution	470 wavelengths	70 frequencies	470 wavelengths	70 frequencies
Size range/resolution	131 sizes from 2 to 100 000 μm		70 sizes from 2 to 250 000 μm	
Scheme	1) Constant bulk density of 0.1 g cm^{-3}, 2) m–D relation in Thompson et al. (2008), 3) m–D relation in Heymsfield et al. (2004), and 4) m–D relation in Brandes et al. (2007)		Five mass ratios of 0.1–0.9, with an increment of 0.2	10 mass ratios from 0.1 to 1, with an increment of 0.1
Refractive index	At 266 K (Warren and Brandt 2008)	At five temperatures 190, 210, 230, 250, and 270 K (Iwabuchi and Yang 2011)	At 266 K (Warren and Brandt 2008)	At five temperatures 190, 210, 230, 250, and 270 K (Iwabuchi and Yang 2011)

size measure that describes ice cloud bulk optical properties, which is independent of particle size distribution details (Wyser and Yang 1998):

$$r_{\text{eff}} = \frac{3\int_{D_{\min}}^{D_{\max}} V(D)N(D)\,dD}{4\int_{D_{\min}}^{D_{\max}} A(D)N(D)\,dD}, \tag{3}$$

where $V(D)$ and $A(D)$ are the volume and projected cross-sectional area of the particles in the size interval D to $D + dD$. The $D_{\min}$ and $D_{\max}$ are the low and upper limits of D, respectively. As documented in Table 2, $D_{\min} = 2$ μm and $D_{\max} = 100\,000$ μm in the present snow database. However, microphysics schemes often do not specify the snow particle shape (Thompson et al. 2008) and hence cannot provide $V(D)$ and $A(D)$ for the r_{eff} computation. The mean particle size measure that microphysics schemes can provide is the ratio of the third to the second moments of a given $N(D)$:

$$r_{\text{eff},p} = \frac{1\int_{D_{\min}}^{D_{\max}} D^3N(D)\,dD}{2\int_{D_{\min}}^{D_{\max}} D^2N(D)\,dD}. \tag{4}$$

We call $r_{\text{eff},p}$, defined in Eq. (4), the effective radius parameter. Bulk hydrometeor optical properties are precalculated at 10 $r_{\text{eff},p}$ values in the MW in CRTM 2.4.0 (Stegmann et al. 2018), which is adopted to test the present snow optical parameterization. If the development of a snow bulk optical parameterization focuses on its consistency with a microphysics scheme, then the snow bulk optical properties should be computed at values of some mean particle size measure that the microphysics scheme can provide. Therefore, we compute the snow MW bulk optical properties at the 10 $r_{\text{eff},p}$ values. The snow particle distribution of Field et al. (2005) is adopted in the Thompson scheme:

$$N(D) = \frac{M_2^4}{M_3^3}\left[k_0 e^{-(M_2/M_3)\Lambda_0 D} + k_1\left(\frac{M_2}{M_3}D\right)^{\mu_s} e^{-(M_2/M_3)\Lambda_1 D}\right], \tag{5}$$

where $k_0 = 490.6$, $k_1 = 17.46$, $\Lambda_0 = 20.78$, $\Lambda_1 = 3.29$, $\mu_s = 0.6357$, and M_n is the nth moment of the distribution. In the snow bulk optical parameterization, the size distribution in Eq. (5) is applied to our snow optical model satisfying the m–D relation in Eq. (2), such that the derived snow bulk optical properties are consistent with the Thompson microphysics scheme. First, $N(D)$ in Eq. (5) is normalized by M_0:

$$M_0 = \int_0^{\infty} N(D)\,dD = \frac{M_2^3}{M_3^2}\left[\frac{k_0}{\Lambda_0} + \frac{k_1}{\Lambda_1^{\mu_s+1}}\Gamma(\mu_s + 1)\right] = 25.84\frac{M_2^3}{M_3^2}, \tag{6}$$

$$N_n(D) = \frac{N(D)}{M_0} = \frac{1}{51.68 r_{\text{eff},p}}\left[k_0 e^{-\Lambda_0 D/(2r_{\text{eff},p})} + k_1\left(\frac{D}{2r_{\text{eff},p}}\right)^{\mu_s} e^{-\Lambda_1 D/(2r_{\text{eff},p})}\right], \tag{7}$$

where $N_n(D)$ is the normalized snow particle size distribution. Notice that $r_{\text{eff},p} = M_3/2M_2$. Furthermore, snow bulk optical properties in the MW are derived with $N_n(D)$ and the single-scattering properties of the snow model (e.g., Baum et al. 2005b; Hong et al. 2009a) at the 10 $r_{\text{eff},p}$ values of interest (Table 3):

$$\beta_{\text{ext},m} = \frac{\int_{D_{\min}}^{D_{\max}} Q_{\text{ext}}(D)A(D)N_n(D)\,dD}{\rho_0\int_{D_{\min}}^{D_{\max}} V(D)N_n(D)\,dD}, \tag{8}$$

TABLE 3. The 10 $r_{\text{eff},p}$ values at which snow MW bulk optical properties are computed and the corresponding r_{eff} values derived from our Thompson-microphysics-scheme-consistent snow optical model.

$r_{\text{eff},p}$ (μm)	r_{eff} (μm)
5	3.43
15	9.82
30	19.30
50	31.95
100	60.72
300	114.56
500	136.85
800	155.84
1000	164.21
1500	178.02

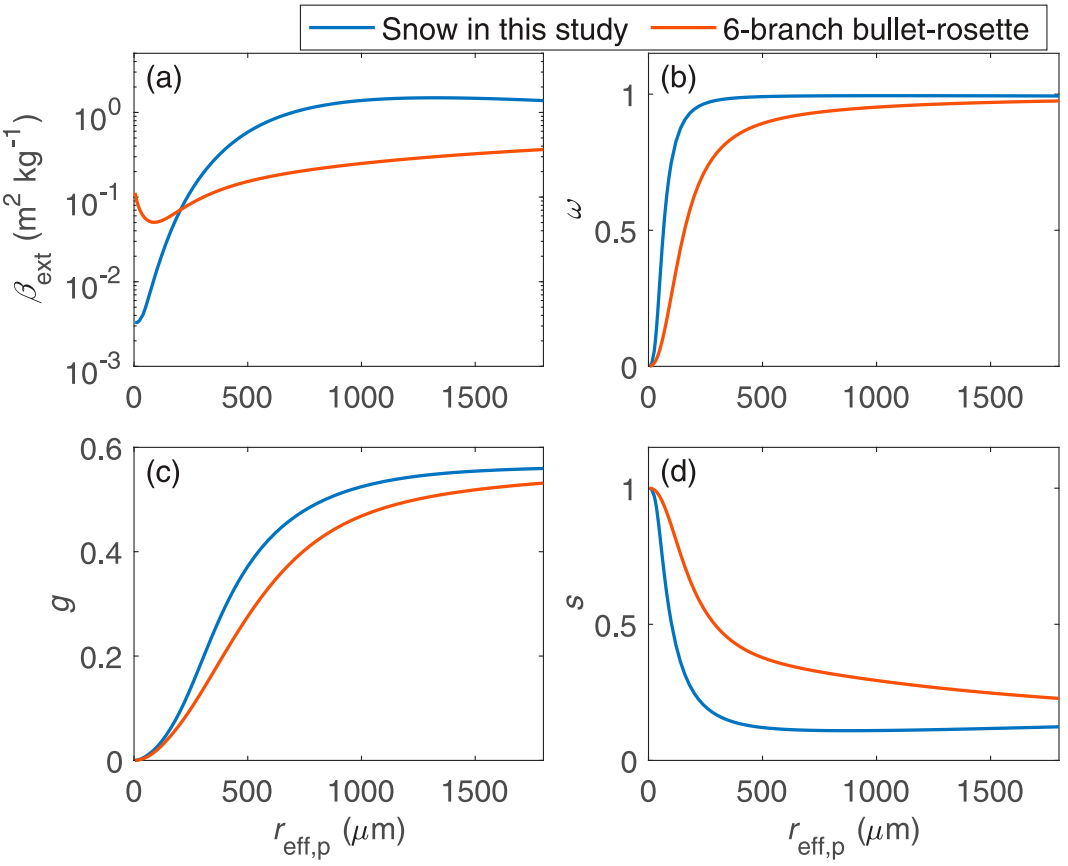

FIG. 2. Bulk (a) mass extinction coefficients β_{ext} (m^2 kg^{-1}), (b) single-scattering albedos ω, (c) asymmetry factors g, and (d) similarity parameters s of the snow optical model in this study (blue) and the 6-branch bullet-rosette model in Ding et al. (2017b) (orange) at 94 GHz and 230 K with the particle size distribution of Field et al. (2005).

$$\omega = \frac{\int_{D_{min}}^{D_{max}} \omega'(D) Q_{ext}(D) A(D) N_n(D)\, dD}{\int_{D_{min}}^{D_{max}} Q_{ext}(D) A(D) N_n(D)\, dD}, \tag{9}$$

$$g = \frac{\int_{D_{min}}^{D_{max}} g'(D)\omega'(D) Q_{ext}(D) A(D) N_n(D)\, dD}{\int_{D_{min}}^{D_{max}} \omega'(D) Q_{ext}(D) A(D) N_n(D)\, dD}, \quad \text{and} \tag{10}$$

$$p(\Theta) = \frac{\int_{D_{min}}^{D_{max}} p'(D,\Theta)\omega'(D) Q_{ext}(D) A(D) N_n(D)\, dD}{\int_{D_{min}}^{D_{max}} \omega'(D) Q_{ext}(D) A(D) N_n(D)\, dD}, \tag{11}$$

where Θ is scattering angle and $\rho_0 = 9.167 \times 10^5$ g m^{-3} is the density of solid ice. The associated r_{eff} values are also documented in Table 3. The δ-fit method (Hu et al. 2000) is used to truncate the phase function to reduce the number of the expansion coefficients required by the CRTM simulation. A truncation angle of 10° is chosen to perform the δ-fit truncation. Given an $r_{eff,p}$ input to CRTM, snow bulk optical properties at this $r_{eff,p}$ are obtained via interpolation in the CRTM simulation.

3. Data and methods

High-frequency (>100 GHz) channels of MW instruments are more sensitive to the scattering of snow particles than low-frequency channels (Bennartz and Bauer 2003; Skofronick-Jackson and Johnson 2011). Yin and Liu (2017) used the BT measurements from the GPM Microwave Imager (GMI) 89 GHz and high-frequency channels to develop an a priori database for snow retrievals over ocean, where the first guess SWC profiles were retrieved from the collocated CPR observations. With the CPR retrieved SWC profiles as the input parameters, Yin and Liu (2019) performed radiation simulations and compared simulated BTs with the measurements of the four GMI high-frequency channels, 166 V, 166 H, 183 ± 3 V, and 183 ± 7 V, where V and H indicate the vertical and horizontal polarization states. The collocated CPR and GPM *Core Observatory* observations during March 2014–August 2016 are provided by a *CloudSat*–GPM coincidence dataset (Turk et al. 2021), which is adopted to test our microphysics-scheme-consistent snow bulk optical parameterization at 230 K as in Yin and Liu (2019). *CloudSat* observations have been used to monitor global snowfall

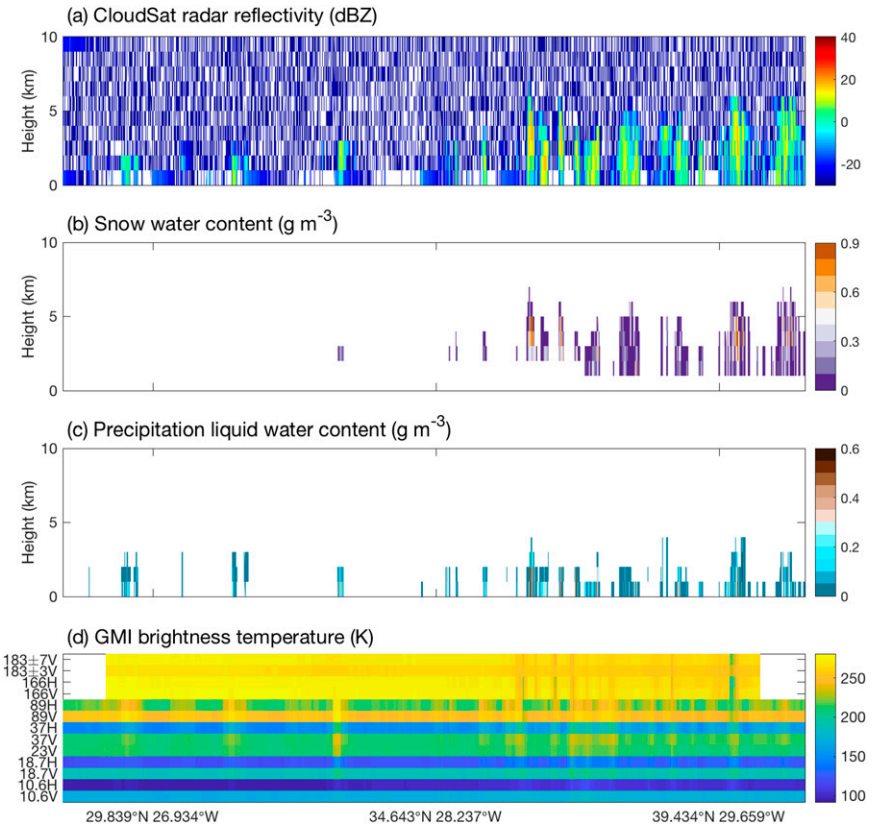

FIG. 3. *CloudSat* (a) 2B-GEOPROF (Marchand et al. 2008) radar reflectivity observations (dBZ), (b) 2C-SNOW-PROFILE snow water content retrievals (g m^{-3}), (c) 2C-RAIN-PROFILE precipitation liquid water content retrievals (g m^{-3}), and (d) collocated GMI brightness temperature measurements (K) along the CPR ground track over the North Atlantic Ocean on 18 Nov 2014.

(Kulie et al. 2020) and validate the CRTM (Chen et al. 2008). Based on the optimal estimation method, snowfall rate and SWC profiles are retrieved using the CPR radar reflectivity and the a priori knowledge of snow microphysical properties (Wood et al. 2013, 2014). This snow retrieval method has also been applied to aircraft W-band radar reflectivity measurements (Heymsfield et al. 2016). *CloudSat* snow retrievals are saved in the 2C-SNOW-PROFILE product, included in the *CloudSat*–GPM coincidence dataset.

Within each GMI field of view (FOV), all the collocated CPR rays are regarded as independent columns to perform CRTM simulations as in Chen et al. (2008), and the average of the simulated BTs is compared with the GMI observation. Horizontal radiation transfer (Kummerow and Weinman 1988) within the GMI FOV is therefore ignored in the BT computation. Each CPR ray has 125 vertical layers with layer heights of about 240 m. The 2nd to the 104th layers (from top to bottom above sea level) are input to the CRTM simulations, resulting in a model top of the atmosphere near 25 km. In each layer, pressure, temperature, and water vapor mass mixing ratio are from the auxiliary ECWMF data included in the coincidence dataset. The ozone volume mixing ratio is derived from version 5 of the ECMWF atmospheric reanalysis (ERA5; Hersbach et al. 2020) monthly mean ozone data. The ERA5 ozone profile closest to each CPR ray is used to calculate the ozone volume mixing ratios in the CPR layers via spline interpolation. Above the freezing level, the solid hydrometeor is treated as snow, whose mass or second moment of the size distribution M_2 is described using the 2C-SNOW-PROFILE SWC retrievals. In each layer, $r_{\mathrm{eff},p}$ is estimated using $r_{\mathrm{eff},p} = M_3/(2M_2)$, where M_3 is calculated using the relation of the size distribution moments [Eqs. (C9)–(C11) in Thompson et al. 2008]. The liquid hydrometeor is treated as rain, whose mass is described using the 2C-RAIN-PROFILE (L'Ecuyer and Stephens 2002; Lebsock and L'Ecuyer 2011; Mitrescu et al. 2010) precipitation liquid water content (PLWC). The 2C-RAIN-PROFILE data have been extensively used in warm rain studies (e.g., Rapp 2016; Rapp et al. 2013; Sun et al. 2022). However, it is difficult to estimate the rain effective radius, because the number concentration of rain droplets, often a prognostic of microphysics schemes, is unstated. Kobayashi (2007) showed a rain droplet effective radius mode of 17 μm derived from TRMM PR and visible and infrared scanner (VIRS) measurements, although the largest droplet sizes might be underestimated due to the observational limit. We simply set the rain effective radius to a constant value of 20 μm in the CRTM simulations.

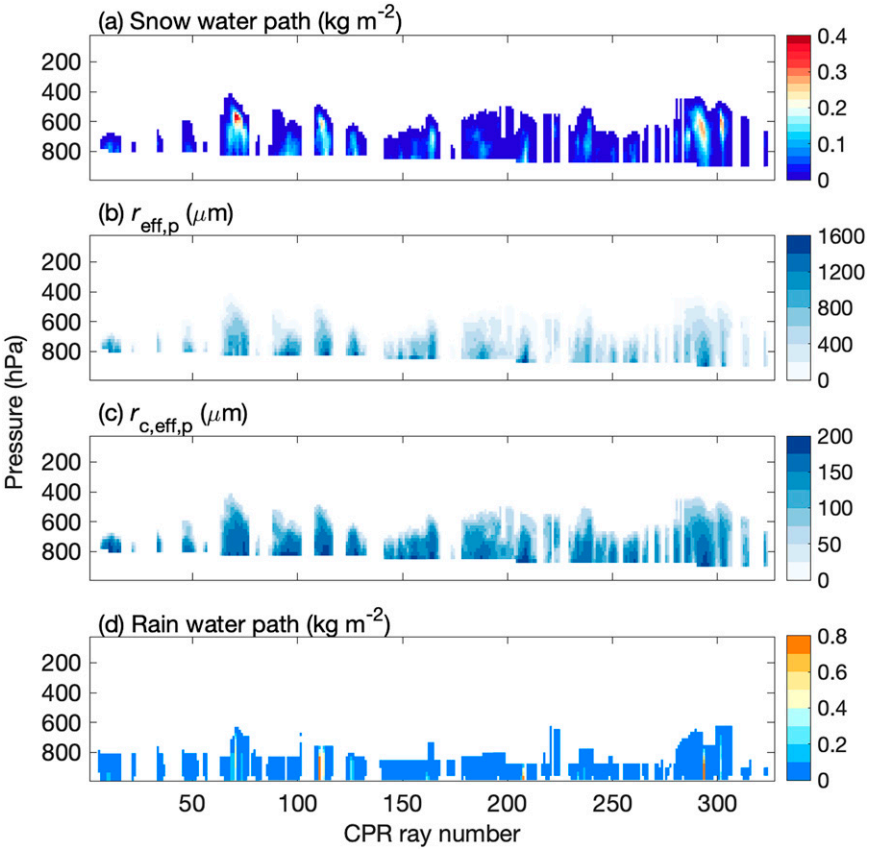

FIG. 4. Profiles of (a) snow water path (kg m^{-2}), (b) snow effective radius $r_{eff,p}$ (μm), (c) corrected snow effective radius $r_{c,eff,p}$ (μm), and (d) rainwater path (kg m^{-2}) for the CPR rays whose collocated GMI FOVs have snow in Fig. 3.

Previous studies showed that the assumptions involved in computing snow single-scattering properties contribute to the uncertainties of *CloudSat* snow retrievals (e.g., Hiley et al. 2011; Kulie and Bennartz 2009; Liu 2008a). For instance, because backscattering cross sections of bullet-rosettes are significantly smaller than those of columns of the same maximum dimension (Hong 2007a; Kulie and Bennartz 2009), given the same radar reflectivity, a significantly higher snow rate will be retrieved if snowflakes are assumed to be bullet-rosettes than if they are assumed to be columns (Hiley et al. 2011). The shape of snowflakes in the 2C-SNOW-PROFILE snow retrieval algorithm was selected based on the ground-based 95-GHz profiling radar near-surface radar reflectivity observations during the Canadian *CloudSat/CALIPSO* Validation Project (C3VP; Hudak et al. 2006). Among a few snowflake shapes that satisfy retrieved m–D and horizontally projected area (A_p)–D relations in Wood et al. (2015), the 8-branch bullet-rosette (8BR) showed the best agreement with the 95-GHz radar near-surface reflectivity observations during the C3VP and hence was adopted in the 2C-SNOW-PROFILE snow retrieval algorithm. Although a single snowflake shape was assumed in the snow retrieval algorithm, Wood et al. (2015) suggested that the near-surface radar reflectivity could also be produced via a combination of one snow shape at small sizes and the other at large sizes, the method we adopt in designing our snow optical model.

The extinction efficiency of columns is about 3–4 times as large as that of bullet-rosettes of the same maximum dimension at 94 GHz (Ding et al. 2017b) and 340 GHz (Hong 2007b). If the 2C-SNOW-PROFILE SWC retrievals are directly used to perform CRTM simulations with our snow bulk optical parameterization, the simulated BTs at the GMI high-frequency channels will be greatly underestimated in high SWC conditions (not shown). Kulie et al. (2010) also reported negative 157-GHz BT biases of column ice optical models when the BT simulations were based on the derived ice water content ensemble from W-band radar reflectivity using different ice optical models. In addition, passive MW solid hydrometeor retrievals are also sensitive to the particle shape assumption (e.g., Evans and Stephens 1995a,b). However, Yin and Liu (2019) reported smaller than 1–3-K biases between simulated and observed GMI high-frequency BTs, when a consistent snow optical model was used in both the forward radiative transfer simulation and the radar retrieved snow description. To avoid the technical problems—such as radar attenuation, multiple scattering, surface clutter, and mixed phase radar gate—in CPR snow retrievals, we choose not to perform snow retrievals with our snow optical model by ourselves.

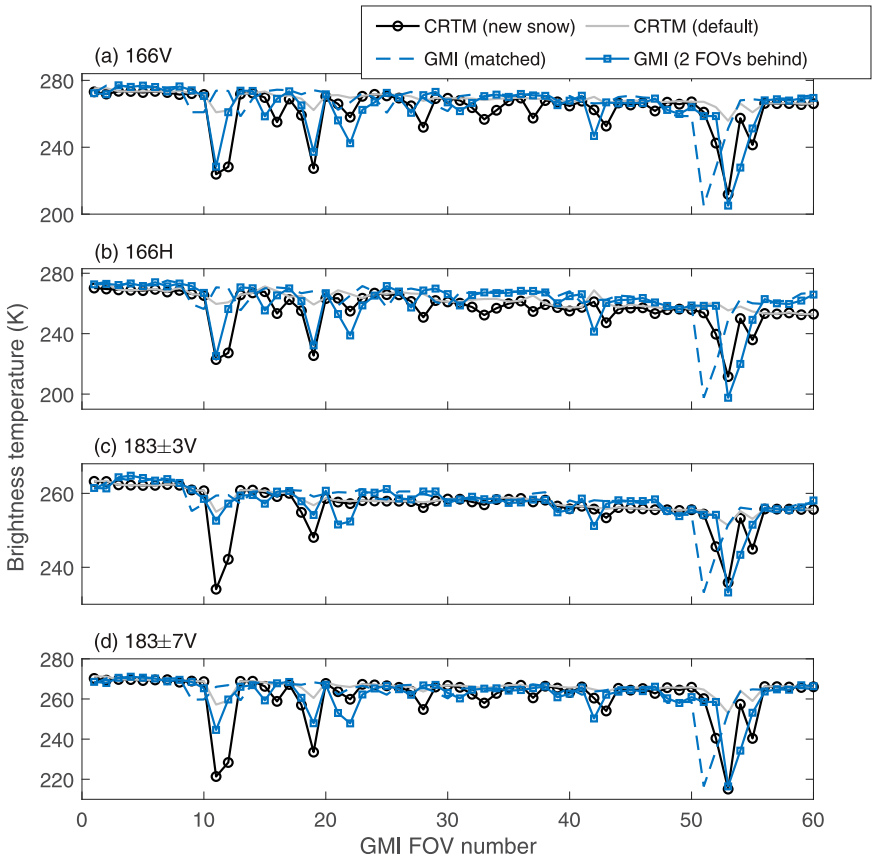

FIG. 5. High-frequency channel brightness temperatures (K) from the CRTM simulations with the new (black) and default (gray) snow optical parameterization schemes, matched GMI observations (dashed blue), and GMI observations 2 FOVs behind (blue) for the GMI FOVs that have snow in Fig. 3.

Instead, we first roughly estimate what snow $r_{\mathrm{eff},p}$ is necessary to produce a radiation field similar with the observed, if the present snow optical model were used in the CPR snow retrievals.

Two scattering media have similar radiation fields if both media have a conserved similarity parameter s defined as follows (van de Hulst 1974):

$$s = \sqrt{\frac{1-\omega}{1-\omega g}}. \tag{12}$$

When s is conserved, the Moderate Resolution Imaging Spectroradiometer (MODIS) Collections 5 and 6 ice cloud optical models (Baum et al. 2005a; Platnick et al. 2017) result in highly agreeing reflectance calculations in MODIS band 7 (Ding et al. 2017a), the near-infrared band in MODIS ice cloud r_{eff} retrievals over oceans. We want to find a corrected snow effective radius parameter $r_{c,\mathrm{eff},p}$ such that the s of our snow model at $r_{c,\mathrm{eff},p}$ is the same as that of the 2C-SNOW-PROFILE 8BR model at $r_{\mathrm{eff},p}$ at 94 GHz (W band). However, the single-scattering properties of the 2C-SNOW-PROFILE 8BR model are not publicly accessible. Knowing that the single-scattering properties of 6-branch and 8-branch bullet rosettes are similar (Aydin and Walsh 1999; Yang et al. 2004), the 6BR model in Ding et al. (2017b) is used instead in correcting the snow $r_{\mathrm{eff},p}$. The single-scattering properties of the 6BR model at 94 GHz are recalculated at the 189 sizes adopted by our new snow database. The snow particle size distribution in the 2C-SNOW-PROFILE 8BR model is also not publicly accessible. We therefore derive the 6BR model bulk optical properties using $N_n(D)$ in Eq. (7). Figure 2 shows a comparison of the bulk optical properties of our snow model and the 6BR model at 94 GHz and 230 K. The β_{ext} of our snow model is nearly an order-of-magnitude greater than that of the 6BR model when $r_{\mathrm{eff},p} > 500$ μm and smaller than that of the 6BR model when $r_{\mathrm{eff},p} < 100$ μm (Fig. 2a). Our snow model shows larger ω and g than the 6BR model (Figs. 2b,c), resulting in a large difference in s between the two models

TABLE 4. RMSEs and MBEs of the CRTM simulated BTs of the four GMI high-frequency channels over the 265 147 clear-sky GMI FOVs over ice-free oceans.

	166 V	166 H	183 ± 3 V	183 ± 7 V
RMSE (K)	3.2	7.3	1.8	2.5
MBE (K)	−0.6	−4.1	0.0	1.1

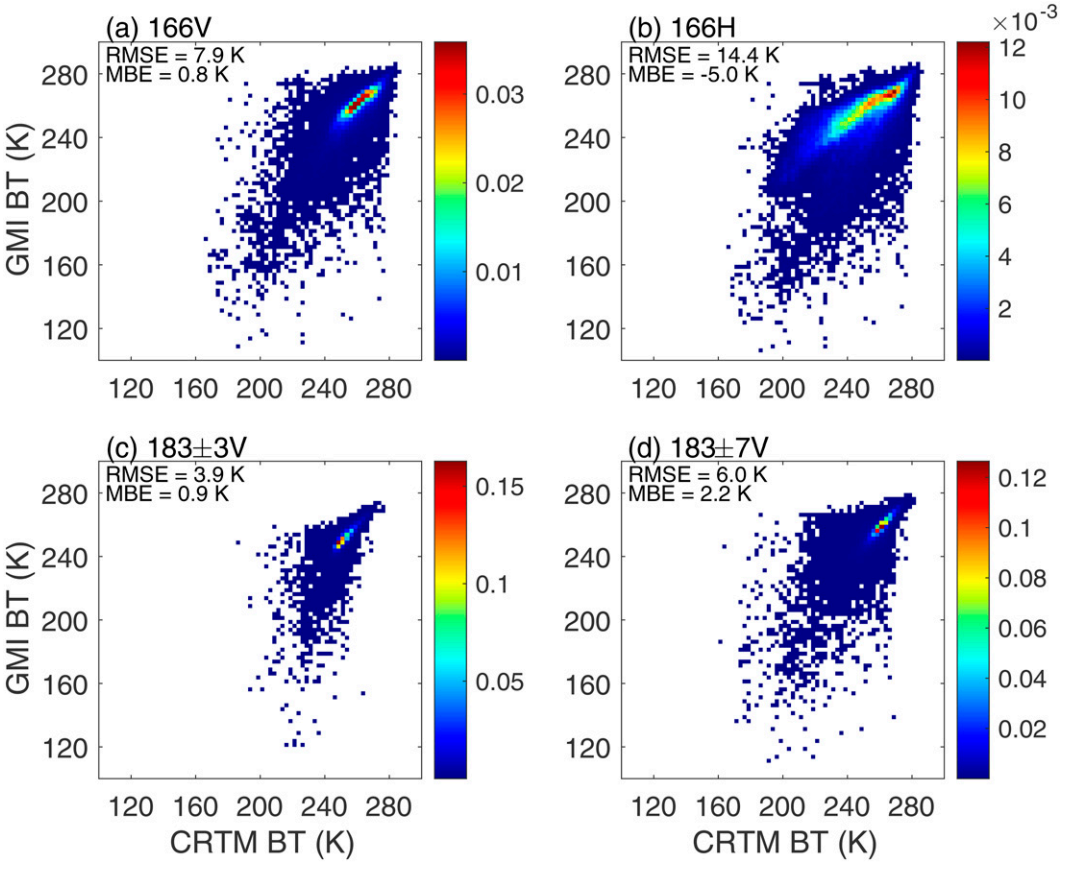

FIG. 6. Scatterplots of the observed vs simulated BTs of the four GMI high-frequency channels for all of the 70 800 selected ice-free oceanic GMI FOVs. Color shows the occurrence frequency in each 2.5-K bin.

(Fig. 2d). Thus, with the variations of s with respect to $r_{\text{eff},p}$ of the two models in Fig. 2d, $r_{c,\text{eff},p}$ can be obtained by solving

$$s(r_{c,\text{eff},p}) = s_{6\text{BR}}(r_{\text{eff},p}), \tag{13}$$

where s and $s_{6\text{BR}}$ are the similarity parameters of our snow model and the 6BR model at 94 GHz and 230 K, respectively.

In the CRTM simulations, the default advanced doubling-adding (ADA) solver (Liu and Weng 2006) is selected with the number of streams (or Gaussian quadrature points) set to 8. The ADA solver also includes two additional streams at the sensor viewing angle in the upper and lower hemispheres, respectively, which, however, are not counted in the number of streams. The viewing angles of the GMI low- and high-frequency channels are 52.78° and 49.11° (Petty and Bennartz 2017). With the GMI orbit height of 407.16 km, the scan (off-nadir) angles of the low- and high-frequency channels are 48.46° and 45.28°. The CRTM simulations include only the GMI FOVs that have CPR snow retrievals over oceans, the emissivity of which is described using the FAST microwave Emissivity Model (FASTEM; Kazumori and English 2015; Liu et al. 2011) version 6. The monthly bootstrap sea ice concentration data (Comiso 2017) are used to remove the FOVs with sea ice. However, the influence of sea ice on the CRTM simulations cannot be completely removed based on the sea ice data. Therefore, we also include a comparison of CRTM simulated and GMI observed BTs over the clear-sky FOVs to quantify the sea ice influence not removed.

4. Results

a. A case over the North Atlantic Ocean

In the CRTM simulations, the snow description is based on *CloudSat* observations. Figure 3 shows the collocated CPR and GMI observations along a CPR ground track segment over the North Atlantic Ocean on 18 November 2014. In the northern portion of the segment, deep convective cores are detected by the CPR with significant radar reflectivity reaching 6 km (Fig. 3a). Within the deep convective cores, CPR snow retrievals are above 1 km with maximum retrieved SWCs between 3 and 5 km (Fig. 3b). Hydrometeors in the *CloudSat* bins are treated as snow and rain and described using the SWC and PLWC retrievals, respectively. As shown in Figs. 3c and 3d, relative to the adjacent clear-sky areas, liquid precipitation enhances the BTs of GMI low-frequency (i.e., 10.6 V, 10.6 H, 18.7 V, 18.7 H, 23 V, 37 V, 37 H, 89 V, and 89 H) channels because of emission from liquid

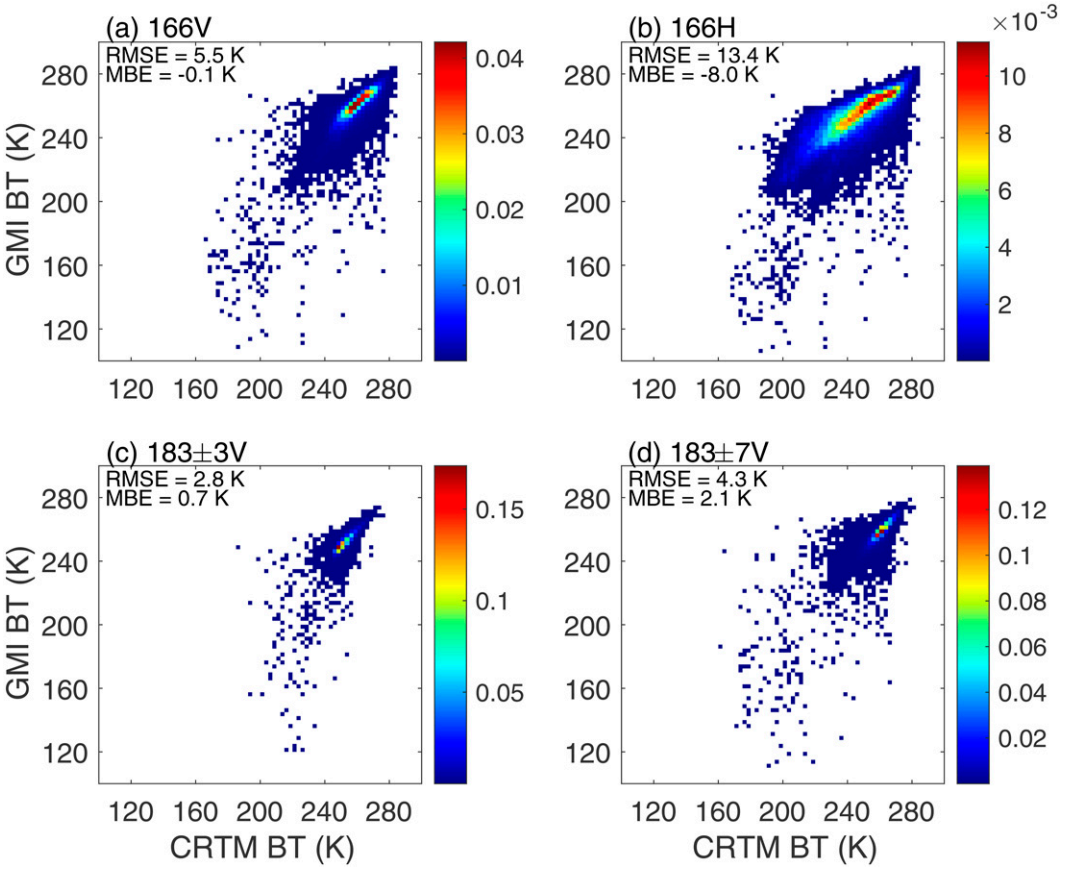

FIG. 7. As in Fig. 6, but for the 57 991 ice-free oceanic GMI FOVs that have no heavy rain.

(Kummerow and Weinman 1988; Wilheit et al. 1977). As shown in Figs. 3b and 3d, the scattering of snowflakes reduces the BTs of GMI high-frequency channels. However, a time offset up to 15 min exists between collocated CPR and GMI observations in the coincidence dataset (Turk et al. 2021). For the selected case shown in Fig. 3, the time offset is 560 s. In Fig. 3, the GMI high-frequency channel BT minima do not exactly overlap with the CPR SWC maxima, suggestive of movement of the detected storms during the 560-s period.

The GMI FOVs with CPR snow retrievals are used to test our microphysics-scheme-consistent snow bulk optical parameterization via CRTM simulations. Figure 4 shows the snow mass and size and rain mass profiles for CRTM simulations using the CPR rays within the GMI FOVs that have snow in Fig. 3. In each *CloudSat* bin, the snow water path (SWP) is the product of the SWC retrieval and the bin thickness; the rainwater path is the product of the PLWC retrieval and the bin thickness. The rainwater paths are generally small and below 0.1 kg m^{-2} with the exceptions in the CPR rays that also have large SWPs around 600 hPa (Figs. 4a,d). The estimated snow $r_{\mathrm{eff},p}$ and $r_{c,\mathrm{eff},p}$ generally decrease with height (Figs. 4b,c). Snow $r_{c,\mathrm{eff},p}$ is smaller than $r_{\mathrm{eff},p}$ (Figs. 4b,c) as expected (Fig. 2d). Not shown in Fig. 4 is the assumed constant raindrop effective radius of 20 μm, as previously mentioned in section 3.

Figure 5 compares the CRTM simulated and observed BTs for the GMI high-frequency channels. It appears that the CRTM simulated BTs agree better with the GMI observations 2 FOVs behind than at the matched GMI observations (Fig. 5). The result suggests that the frozen hydrometeors associated with the detected storms move about 2 GMI FOVs during the 560-s time offset between the collocated CPR and GMI observations. Mismatches between the atmospheric states observed by CPR and GMI also occurred because of the different view angles of the two instruments. We therefore compare the GMI observations up to 4 FOVs ahead and behind the matched ones in each 15-min coincidence data segment with the CRTM simulations and identify the observations that agree best with the simulated 166 V BTs in terms of the root-mean-square error (RMSE). Among the 4 GMI high-frequency channels, the 166 V channel is most sensitive to scattering by snow in the lower and middle troposphere (Yin and Liu 2019). The best agreeing 166 V observation matchups are then used to examine CRTM simulations for all selected cases. The matchups for the clear-sky comparison of CRTM simulated and GMI observed BTs are found in the same way. In addition, the default CRTM snow MW optical properties are computed based on the Lorenz-Mie theory; snow particles are assumed to be spheres with a density of 400 kg m^{-3} and satisfy a modified gamma size distribution (Geer et al. 2018). Given

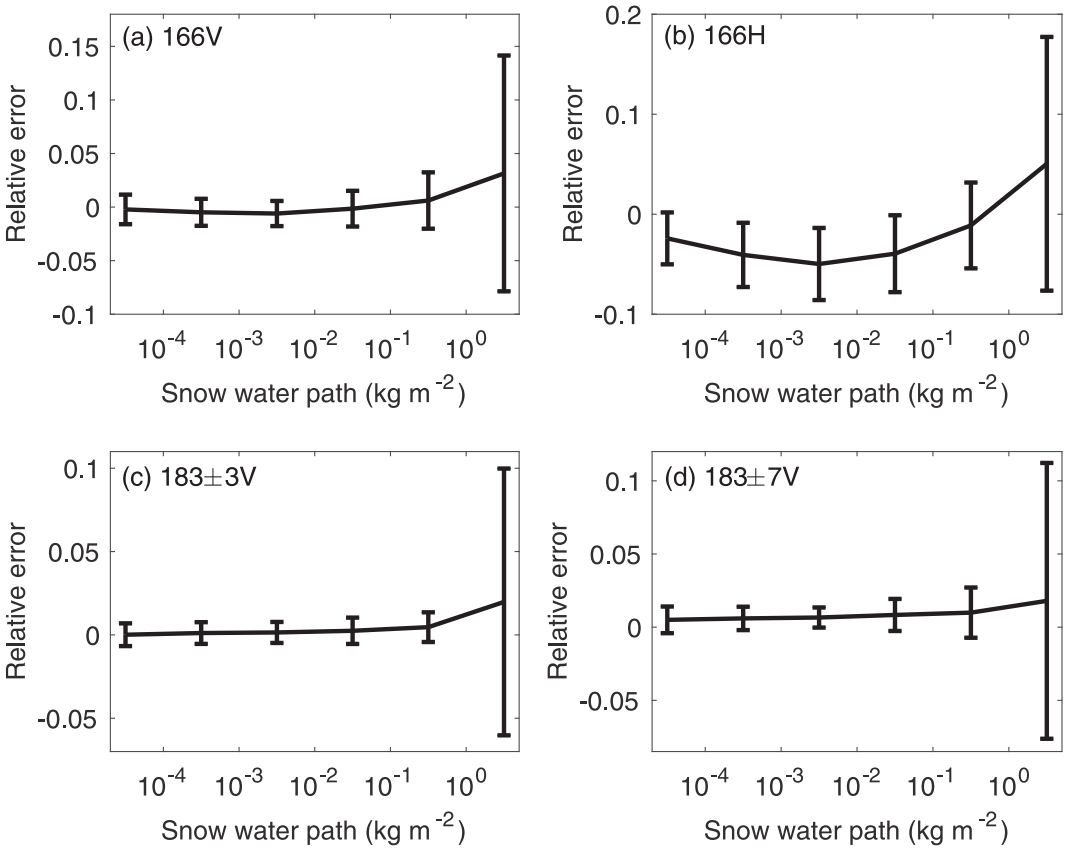

FIG. 8. Mean relative errors of the simulated GMI high-frequency BTs in different mean column SWP intervals for the no-heavy-rain ice-free oceanic GMI FOVs. The error bars mark the standard deviations.

the same $r_{\text{eff},p}$, the mass extinction coefficient of the new snow optical parameterization is significantly higher than that of the default one (not shown). As a result, the CRTM simulated BTs with the default snow parameterization are consistently higher than those with the new snow parameterization; the 166 V and 166 H BT differences reach near 45 K over the deep convective core in the 53rd GMI FOV (Fig. 5). In the rest of this study, only the CRTM simulation results with the new snow parameterization are shown.

b. *All cases over the global oceans*

Table 4 documents the simulated clear-sky BT RMSEs and mean bias errors (MBEs) of the 4 GMI high-frequency channels. The 166 H channel shows a clear-sky BT RMSE of 7.3 K (Table 4). Yin and Liu (2019) report the largest clear-sky BT error standard deviation of the 166 H channel among the four GMI high-frequency channels using the same *CloudSat*–GPM coincidence dataset. Sea ice rarely occurs between 40°N and 40°S. If only the ice-free oceanic clear-sky FOVs between 40°N and 40°S are kept, the 166 H BT RMSE reduces from 7.3 to 4.8 K and mean bias error (MBE) increases from −4.1 to −1.5 K, although the BT RMSEs and MBEs of the other three channels almost do not change (not shown). The more accurate clear-sky 166 V BT simulation between 40°N and 40°S suggests that the sea ice influence on this channel is not completely removed with the help of the monthly bootstrap sea ice concentration data. Based on all 70 800 GMI ice-free oceanic FOVs with snow selected for the CRTM simulations, the simulated high-frequency channel BTs have RMSEs of 7.9, 14.4, 3.9, and 6.0 K, respectively (Fig. 6), smaller than the reported 20 K first guess departures in the all-sky data assimilation (Geer and Bauer 2011). If the heavy-rain FOVs are removed by excluding the cases whose mean column rainwater paths are greater than 0.1 kg m^{-2}, the RMSEs decrease to 5.5, 13.4, 2.8, and 4.3 K, respectively (Fig. 7). The 0.1 kg m^{-2} rainwater path is the 59th percentile for the 31 587 FOVs that have liquid precipitation. The result suggests that the constant 20-μm rain effective radius assumption may be problematic for heavy-rain situations. Relative to the Global Precipitation Climatology Project (GPCP; Huffman et al. 2009) data, the *CloudSat* 2C-RAIN-PROFILE underestimates the rainfall over the convergence regions in the southeastern Pacific Ocean, because the heavy rainfall associated with deep convection is likely to saturate the CPR signal (Rapp et al. 2013). Presumably, the CPR signal saturation also contributes to the increased BT uncertainties for the heavy-rain cases in the CRTM simulations in this study.

Let BT relative error be the difference between simulated and observed BTs divided by the simulated BT. Figure 8 shows the mean BT relative errors in different mean column

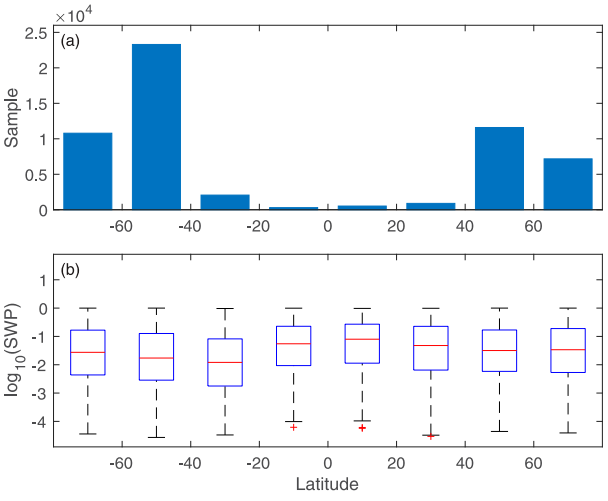

FIG. 9. (a) Latitude distribution of the 56 645 ice-free oceanic GMI FOVs that have no heavy rain or snow. (b) Boxplots of the logarithm base 10 of the mean column SWPs of the samples in different latitude belts. The red lines and pluses mark the medians and outliers, respectively. The box top and bottom edges mark the 75th and 25th percentiles, respectively. The whiskers extend to the extremes.

SWP intervals. When the mean column SWP is greater than 1 kg m^{-2}, the CRTM simulations significantly overestimate the GMI high-frequency BTs (Fig. 8), presumably due to radar signal saturation as in the heavy-rain situations. Relative to the Multi-Radar Multi-Sensor (MRMS) system observations (Zhang et al. 2016), the 2C-SNOW-PROFILE underestimates snowfall rates in heavy-snow situations (Cao et al. 2014; Mroz et al. 2021). The 1 kg m^{-2} mean column SWP is the 98th percentile for the 57 991 FOVs that have no heavy rain. If the heavy-snow cases that have SWPs greater than 1 kg m^{-2} are removed from the no-heavy-rain FOVs, the remaining no-heavy-rain-or-snow FOVs sum to 56 645. As shown in Fig. 9a, most of the no-heavy-rain-or-snow samples are over the extratropics. The median SWP is highest between 0° and 20°N and lowest between 40° and 20°S during the period (Fig. 9b). The mean relative errors of the simulated BTs over the no-heavy-rain-or-snow ice-free oceanic GMI FOVs are generally closer to 0 over the middle and high latitudes than over the tropics (Fig. 10). The northern and southern boundaries of the GMI FOVs in the coincidence dataset are about 69°N and 69°S, respectively. The CRTM BT overestimation shown in Fig. 10 may be suggestive of a SWC underestimation over the tropics, although the BT overestimation may also result from other unknown uncertainty sources. Perhaps, the quality of the 2C-SNOW-PROFILE snow retrievals varies with latitude. While numerous studies have evaluated the 2C-SNOW-PROFILE snow retrievals over middle and high latitudes (e.g., Cao et al. 2014; Chen et al. 2016; Matrosov 2019; Mroz et al. 2021; Norin et al. 2015; Souverijns et al. 2018), evaluations over the tropics are scarce. If attenuation and multiple scattering are ignored, lack of prior knowledge of the snow size distribution parameters is believed to be the greatest uncertainty source of the W-band radar snow mass retrievals (Wood and L'Ecuyer 2021). With the tropical cases between 20°N and 20°S farther removed from the FOVs with no heavy rain or snow, the resulting 55 821 samples have simulated high-frequency BT RMSEs reduced to 4.3, 13.0, 1.8, and 3.3 K, respectively; the BT MBEs of the samples are −0.4, −8.7, 0.6, and 2.0 K, respectively. The agreement between the CRTM simulated and GMI observed BTs suggests the potential of applying our microphysics-scheme-consistent snow optical parameterization in all-sky data assimilations.

5. Conclusions

The data assimilation community requires consistency in the assumed hydrometeor *m–D* relation and the particle size distribution between the forecast model and observation operator. Motivated by this requirement, we developed a microphysics-scheme-consistent snow and graupel single-scattering database. In this database, snowflakes are assumed to be a mixture of randomly oriented hexagonal columns and dendrite aggregates with an equal number of mirror-imaging orientations, the mixing ratios of which can be adjusted to satisfy a given *m–D* relation in each particle size range. Snow assumptions in the Thompson microphysics scheme are then used to illustrate how microphysics-scheme-consistent snow bulk optical properties may be derived. Furthermore, the Thompson-scheme-consistent snow bulk optical parameterization in the MW is incorporated into CRTM 2.4.0 for a test. With the CPR snow and liquid precipitation retrievals as the input, the CRTM with the new snow parameterization is used to simulate BTs of the collocated GMI 4 high-frequency channels 166 V, 166 H, 183 ± 3 V, and 183 ± 7 V. The simulated 166 V, 183 ± 3 V, and 183 ± 7 V BTs show RMSEs smaller than 5 K over the global extratropical and polar ice-free oceans, if heavy-rain and heavy-snow cases are excluded because of possible radar signal saturation. However, the 166 H channel shows a BT RMSE of 13 K. A large portion of the outliers do not appear to be near the known sea ice (not shown). Hence, the 166 H channel uncertainty is presumably due to the mismatches between the atmospheric states observed by CPR and GMI. Among the four channels, the 166 H also has the largest BT RMSE of 7.3 K in the clear-sky condition (Table 4). In addition, the 166 H channel BT is thought to be sensitive to atmospheric liquid precipitation emission (Yin and Liu 2019), which can mask the snow scattering signal (Liu and Seo 2013; Wang et al. 2013). In the CRTM simulations in this study, the 2C-RAIN-PROFILE PLWC is used to describe the liquid water content that contributes to the signals of the 4 GMI high-frequency channels. The 166 H BT underestimation in this study (Figs. 6b–8b) may be due to the underestimation of the liquid water content underneath snow by the 2C-RAIN-PROFILE PLWC. In this study, randomly orientated particles are assumed in the new snow model and hydrometeor polarization is not included in the CRTM 2.4.0 radiative solver. The lack of particle orientation and polarization may contribute to the simulation errors at 166 GHz. The agreement between the GMI high-frequency BT simulations and observations

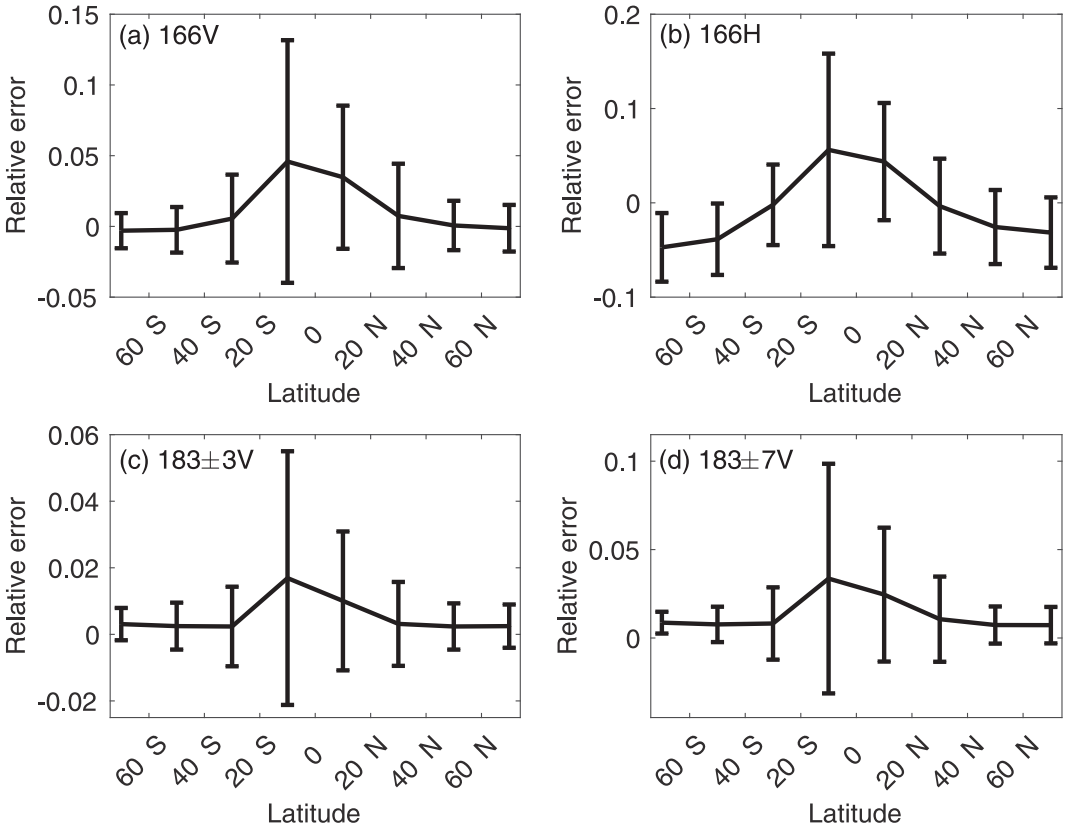

FIG. 10. Mean relative errors of the simulated GMI high-frequency BTs in different latitudinal belts for the no-heavy-rain-or-snow ice-free oceanic GMI FOVs. The error bars mark the standard deviations.

suggests the possibility of all-sky data assimilation applications of our microphysics-scheme-consistent snow and graupel database. In the future, the new snow optical parameterization will be tested within the framework of a numerical weather prediction model. In this study, only snow bulk optical properties at 230 K are tested. The optical properties at other temperatures available in this database will be examined in future studies. In addition, melted and dry snow particles show distinct scattering and extinction properties (Johnson et al. 2016). The influence of melting is not considered in our snow optical model. Future studies will investigate whether the dry snow optical model may be replaced by a melted snow optical model in the melting layer in radar snow retrievals and MW imager signal simulations.

Acknowledgments. This study was supported by NOAA Contract 1332KP20PNEED0096. Author Ping Yang also acknowledges the support of the endowment funds related to the David Bullock Harris Chair in Geosciences (02-512231-10000) at Texas A&M University. The authors thank Joseph Turk for his instructions on using the *CloudSat*–GPM coincidence dataset. We thank Steven Schroeder for helping to edit the paper. We are grateful for encouragement from the editor Matthew Kumjian and the constructive comments from three anonymous reviewers. The snow and graupel single-scattering properties were computed using the Texas A&M High Performance Research Computing (HPRC) and the NOAA Orion supercomputers. The CRTM simulations in this study were performed with the advanced computing resources provided by the Texas A&M HPRC. The views, opinions, and findings contained in this report are those of the authors and should not be construed as an official NOAA or U.S. government position, policy, or decision.

Data availability statement. The CRTM 2.4.0 model code was accessed from the Joint Center for Satellite Data Assimilation (https://github.com/JCSDA/crtm). *CloudSat*–GPM coincidence data were downloaded from the NASA Earth Observing System Data and Information System (EOSDIS; https://arthurhouhttps.pps.eosdis.nasa.gov/text/gpmdata/). ERA5 monthly ozone data were downloaded from the Climate Data Store (https://cds.climate.copernicus.eu/). The monthly bootstrap sea ice concentration data were downloaded from the NASA National Snow and Ice Data Center Distributed Active Archive Center (https://nsidc.org/data/nsidc-0079/versions/3). The snow single-scattering database introduced in this study is available online (https://doi.org/10.18738/T8/LGJ9SA).

REFERENCES

Austin, R. T., A. J. Heymsfield, and G. L. Stephens, 2009: Retrieval of ice cloud microphysical parameters using the CloudSat millimeter-wave radar and temperature. *J. Geophys. Res.*, **114**, D00A23, https://doi.org/10.1029/2008JD010049.

Aydin, K., and T. M. Walsh, 1999: Millimeter wave scattering from spatial and planar bullet rosettes. *IEEE Trans. Geosci. Remote Sens.*, **37**, 1138–1150, https://doi.org/10.1109/36.752232.

Baran, A. J., 2012: From the single-scattering properties of ice crystals to climate prediction: A way forward. *Atmos. Res.*, **112**, 45–69, https://doi.org/10.1016/j.atmosres.2012.04.010.

——, P. Hill, K. Furtado, P. Field, and J. Manners, 2014: A coupled cloud physics–radiation parameterization of the bulk optical properties of cirrus and its impact on the Met Office Unified Model Global Atmosphere 5.0 configuration. *J. Climate*, **27**, 7725–7752, https://doi.org/10.1175/JCLI-D-13-00700.1.

Barlakas, V., A. J. Geer, and P. Eriksson, 2021: Introducing hydrometeor orientation into all-sky microwave and submillimeter assimilation. *Atmos. Meas. Tech.*, **14**, 3427–3447, https://doi.org/10.5194/amt-14-3427-2021.

Bauer, P., A. J. Geer, P. Lopez, and D. Salmond, 2010: Direct 4D-Var assimilation of all-sky radiances. Part I: Implementation. *Quart. J. Roy. Meteor. Soc.*, **136**, 1868–1885, https://doi.org/10.1002/qj.659.

——, and Coauthors, 2011: Satellite cloud and precipitation assimilation at operational NWP centres. *Quart. J. Roy. Meteor. Soc.*, **137**, 1934–1951, https://doi.org/10.1002/qj.905.

Baum, B. A., A. J. Heymsfield, P. Yang, and S. T. Bedka, 2005a: Bulk scattering properties for the remote sensing of ice clouds. Part I: Microphysical data and models. *J. Appl. Meteor. Climatol.*, **44**, 1885–1895, https://doi.org/10.1175/JAM2308.1.

——, P. Yang, A. J. Heymsfield, S. Platnick, M. D. King, Y.-X. Hu, and S. T. Bedka, 2005b: Bulk scattering properties for the remote sensing of ice clouds. Part II: Narrowband models. *J. Appl. Meteor. Climatol.*, **44**, 1896–1911, https://doi.org/10.1175/JAM2309.1.

Bennartz, R., and P. Bauer, 2003: Sensitivity of microwave radiances at 85–183 GHz to precipitating ice particles. *Radio Sci.*, **38**, 8075, https://doi.org/10.1029/2002RS002626.

Bi, L., and P. Yang, 2014: Accurate simulation of the optical properties of atmospheric ice crystals with the invariant imbedding T-matrix method. *J. Quant. Spectrosc. Radiat. Transfer*, **138**, 17–35, https://doi.org/10.1016/j.jqsrt.2014.01.013.

Brandes, E. A., K. Ikeda, G. Zhang, M. Schönhuber, and R. M. Rasmussen, 2007: A statistical and physical description of hydrometeor distributions in Colorado snowstorms using a video disdrometer. *J. Appl. Meteor. Climatol.*, **46**, 634–650, https://doi.org/10.1175/JAM2489.1.

Brath, M., R. Ekelund, P. Eriksson, O. Lemke, and S. A. Buehler, 2020: Microwave and submillimeter wave scattering of oriented ice particles. *Atmos. Meas. Tech.*, **13**, 2309–2333, https://doi.org/10.5194/amt-13-2309-2020.

Cao, Q., Y. Hong, S. Chen, J. J. Gourley, J. Zhang, and P. E. Kirstetter, 2014: Snowfall detectability of NASA's CloudSat: The first cross-investigation of its 2C-snow-profile product and National Multi-Sensor Mosaic QPE (NMQ) snowfall data. *Prog. Electromagn. Res.*, **148**, 55–61, https://doi.org/10.2528/PIER14030405.

Chase, R. J., S. W. Nesbitt, and G. M. McFarquhar, 2021: A dual-frequency radar retrieval of two parameters of the snowfall particle size distribution using a neural network. *J. Appl. Meteor. Climatol.*, **60**, 341–359, https://doi.org/10.1175/JAMC-D-20-0177.1.

Chen, S., and Coauthors, 2016: Comparison of snowfall estimates from the NASA CloudSat cloud profiling radar and NOAA/NSSL multi-radar multi-sensor system. *J. Hydrol.*, **541**, 862–872, https://doi.org/10.1016/j.jhydrol.2016.07.047.

Chen, Y., F. Weng, Y. Han, and Q. Liu, 2008: Validation of the community radiative transfer model by using CloudSat data. *J. Geophys. Res.*, **113**, D00A03, https://doi.org/10.1029/2007JD009561.

Comiso, J. C., 2017: Bootstrap sea ice concentrations from *Nimbus-7* SMMR and DMSP SSM/I-SSMIS, version 3. NASA National Snow and Ice Data Center Distributed Active Archive Center, accessed 18 July 2022, https://doi.org/10.5067/7Q8HCCWS4I0R.

Cox, G. P., 1988: Modelling precipitation in frontal rainbands. *Quart. J. Roy. Meteor. Soc.*, **114**, 115–127, https://doi.org/10.1002/qj.49711447906.

Coy, J. J., A. Bell, P. Yang, and D. L. Wu, 2020: Sensitivity analyses for the retrievals of ice cloud properties from radiometric and polarimetric measurements in sub-mm/mm and infrared bands. *J. Geophys. Res. Atmos.*, **125**, e2019JD031422, https://doi.org/10.1029/2019JD031422.

Ding, J., P. Yang, G. W. Kattawar, M. D. King, S. Platnick, and K. G. Meyer, 2017a: Validation of quasi-invariant ice cloud radiative quantities with MODIS satellite-based cloud property retrievals. *J. Quant. Spectrosc. Radiat. Transfer*, **194**, 47–57, https://doi.org/10.1016/j.jqsrt.2017.03.025.

——, L. Bi, P. Yang, G. W. Kattawar, F. Weng, Q. Liu, and T. Greenwald, 2017b: Single-scattering properties of ice particles in the microwave regime: Temperature effect on the ice refractive index with implications in remote sensing. *J. Quant. Spectrosc. Radiat. Transfer*, **190**, 26–37, https://doi.org/10.1016/j.jqsrt.2016.11.026.

Dolinar, E. K., X. Dong, B. Xi, J. H. Jiang, and H. Su, 2015: Evaluation of CMIP5 simulated clouds and TOA radiation budgets using NASA satellite observations. *Climate Dyn.*, **44**, 2229–2247, https://doi.org/10.1007/s00382-014-2158-9.

Ekelund, R., P. Eriksson, and S. Pfreundschuh, 2020: Using passive and active observations at microwave and sub-millimetre wavelengths to constrain ice particle models. *Atmos. Meas. Tech.*, **13**, 501–520, https://doi.org/10.5194/amt-13-501-2020.

Eliasson, S., S. Buehler, M. Milz, P. Eriksson, and V. John, 2011: Assessing observed and modelled spatial distributions of ice water path using satellite data. *Atmos. Chem. Phys.*, **11**, 375–391, https://doi.org/10.5194/acp-11-375-2011.

Eriksson, P., S. A. Buehler, C. P. Davis, C. Emde, and O. Lemke, 2011: ARTS, the atmospheric radiative transfer simulator, version 2. *J. Quant. Spectrosc. Radiat. Transfer*, **112**, 1551–1558, https://doi.org/10.1016/j.jqsrt.2011.03.001.

——, M. Jamali, J. Mendrok, and S. A. Buehler, 2015: On the microwave optical properties of randomly oriented ice hydrometeors. *Atmos. Meas. Tech.*, **8**, 1913–1933, https://doi.org/10.5194/amt-8-1913-2015.

——, R. Ekelund, J. Mendrok, M. Brath, O. Lemke, and S. A. Buehler, 2018: A general database of hydrometeor single scattering properties at microwave and sub-millimetre wavelengths. *Earth Syst. Sci. Data*, **10**, 1301–1326, https://doi.org/10.5194/essd-10-1301-2018.

Evans, K. F., and G. L. Stephens, 1995a: Microwave radiative transfer through clouds composed of realistically shaped ice crystals. Part I: Single scattering properties. *J. Atmos. Sci.*, **52**,

2041–2057, https://doi.org/10.1175/1520-0469(1995)052<2041:MRTTCC>2.0.CO;2.

——, and ——, 1995b: Microweve radiative transfer through clouds composed of realistically shaped ice crystals. Part II: Remote sensing of ice clouds. *J. Atmos. Sci.*, **52**, 2058–2072, https://doi.org/10.1175/1520-0469(1995)052<2058:MRTTCC>2.0.CO;2.

——, and Coauthors, 2012: Ice hydrometeor profile retrieval algorithm for high-frequency microwave radiometers: Application to the CoSSIR instrument during TC4. *Atmos. Meas. Tech.*, **5**, 2277–2306, https://doi.org/10.5194/amt-5-2277-2012.

Ferraro, R. R., and Coauthors, 2005: NOAA operational hydrological products derived from the advanced microwave sounding unit. *IEEE Trans. Geosci. Remote Sens.*, **43**, 1036–1049, https://doi.org/10.1109/TGRS.2004.843249.

Field, P. R., R. J. Hogan, P. R. A. Brown, A. J. Illingworth, T. W. Choularton, and R. J. Cotton, 2005: Parametrization of ice-particle size distributions for mid-latitude stratiform cloud. *Quart. J. Roy. Meteor. Soc.*, **131**, 1997–2017, https://doi.org/10.1256/qj.04.134.

Foot, J. S., 1988: Some observations of the optical properties of clouds. II: Cirrus. *Quart. J. Roy. Meteor. Soc.*, **114**, 145–164, https://doi.org/10.1002/qj.49711447908.

Fox, S., 2020: A evaluation of radiative transfer simulations of cloudy scenes from a numerical weather prediction model at sub-millimetre frequencies using airborne observations. *Remote Sens.*, **12**, 2758, https://doi.org/10.3390/rs12172758.

——, and Coauthors, 2019: Airborne validation of radiative transfer modelling of ice clouds at millimetre and sub-millimetre wavelengths. *Atmos. Meas. Tech.*, **12**, 1599–1617, https://doi.org/10.5194/amt-12-1599-2019.

Galligani, V. S., C. Prigent, E. Defer, C. Jimenez, P. Eriksson, J.-P. Pinty, and J.-P. Chaboureau, 2015: Meso-scale modelling and radiative transfer simulations of a snowfall event over France at microwaves for passive and active modes and evaluation with satellite observations. *Atmos. Meas. Tech.*, **8**, 1605–1616, https://doi.org/10.5194/amt-8-1605-2015.

Geer, A. J., 2021: Physical characteristics of frozen hydrometeors inferred with parameter estimation. *Atmos. Meas. Tech.*, **14**, 5369–5395, https://doi.org/10.5194/amt-14-5369-2021.

——, and P. Bauer, 2011: Observation errors in all-sky data assimilation. *Quart. J. Roy. Meteor. Soc.*, **137**, 2024–2037, https://doi.org/10.1002/qj.830.

——, and F. Baordo, 2014: Improved scattering radiative transfer for frozen hydrometeors at microwave frequencies. *Atmos. Meas. Tech.*, **7**, 1839–1860, https://doi.org/10.5194/amt-7-1839-2014.

——, P. Bauer, and C. W. O'Dell, 2009: A revised cloud overlap scheme for fast microwave radiative transfer in rain and cloud. *J. Appl. Meteor. Climatol.*, **48**, 2257–2270, https://doi.org/10.1175/2009JAMC2170.1.

——, ——, and P. Lopez, 2010: Direct 4D-Var assimilation of all-sky radiances. Part II: Assessment. *Quart. J. Roy. Meteor. Soc.*, **136**, 1886–1905, https://doi.org/10.1002/qj.681.

——, and Coauthors, 2017: The growing impact of satellite observations sensitive to humidity, cloud and precipitation. *Quart. J. Roy. Meteor. Soc.*, **143**, 3189–3206, https://doi.org/10.1002/qj.3172.

——, and Coauthors, 2018: All-sky satellite data assimilation at operational weather forecasting centres. *Quart. J. Roy. Meteor. Soc.*, **144**, 1191–1217, https://doi.org/10.1002/qj.3202.

——, and Coauthors, 2021: Bulk hydrometeor optical properties for microwave and sub-millimetre radiative transfer in RTTOV-SCATT v13. 0. *Geosci. Model Dev.*, **14**, 7497–7526, https://doi.org/10.5194/gmd-14-7497-2021.

Gong, J., and D. L. Wu, 2017: Microphysical properties of frozen particles inferred from Global Precipitation Measurement (GPM) Microwave Imager (GMI) polarimetric measurements. *Atmos. Chem. Phys.*, **17**, 2741–2757, https://doi.org/10.5194/acp-17-2741-2017.

Greenwald, T. J., and Coauthors, 2016: Real-time simulation of the GOES-R ABI for user readiness and product evaluation. *Bull. Amer. Meteor. Soc.*, **97**, 245–261, https://doi.org/10.1175/BAMS-D-14-00007.1.

Han, Y., P. van Delst, Q. Liu, F. Weng, B. Yan, R. Treadon, and J. Derber, 2006: JCSDA Community Radiative Transfer Model (CRTM): Version 1. NOAA Tech. Rep. NESDIS 122, 40 pp.

Hersbach, H., and Coauthors, 2020: The ERA5 global reanalysis. *Quart. J. Roy. Meteor. Soc.*, **146**, 1999–2049, https://doi.org/10.1002/qj.3803.

Heymsfield, A. J., A. Bansemer, C. Schmitt, C. Twohy, and M. R. Poellot, 2004: Effective ice particle densities derived from aircraft data. *J. Atmos. Sci.*, **61**, 982–1003, https://doi.org/10.1175/1520-0469(2004)061<0982:EIPDDF>2.0.CO;2.

——, S. Y. Matrosov, and N. B. Wood, 2016: Toward improving ice water content and snow-rate retrievals from radars. Part I: X and W bands, emphasizing *CloudSat*. *J. Appl. Meteor. Climatol.*, **55**, 2063–2090, https://doi.org/10.1175/JAMC-D-15-0290.1.

Hiley, M. J., M. S. Kulie, and R. Bennartz, 2011: Uncertainty analysis for *CloudSat* snowfall retrievals. *J. Appl. Meteor. Climatol.*, **50**, 399–418, https://doi.org/10.1175/2010JAMC2505.1.

Honeyager, R., G. Liu, and H. Nowell, 2016: Voronoi diagram-based spheroid model for microwave scattering of complex snow aggregates. *J. Quant. Spectrosc. Radiat. Transfer*, **170**, 28–44, https://doi.org/10.1016/j.jqsrt.2015.10.025.

Hong, G., 2007a: Radar backscattering properties of nonspherical ice crystals at 94 GHz. *J. Geophys. Res.*, **112**, D22203, https://doi.org/10.1029/2007JD008839.

——, 2007b: Parameterization of scattering and absorption properties of nonspherical ice crystals at microwave frequencies. *J. Geophys. Res.*, **112**, D11208, https://doi.org/10.1029/2006JD008364.

——, P. Yang, B. A. Baum, A. J. Heymsfield, and K.-M. Xu, 2009a: Parameterization of shortwave and longwave radiative properties of ice clouds for use in climate models. *J. Climate*, **22**, 6287–6312, https://doi.org/10.1175/2009JCLI2844.1.

——, and Coauthors, 2009b: Scattering database in the millimeter and submillimeter wave range of 100–1000 GHz for nonspherical ice particles. *J. Geophys. Res.*, **114**, D06201, https://doi.org/10.1029/2008JD010451.

Hou, A. Y., and Coauthors, 2014: The Global Precipitation Measurement mission. *Bull. Amer. Meteor. Soc.*, **95**, 701–722, https://doi.org/10.1175/BAMS-D-13-00164.1.

Hu, Y.-X., B. Wielicki, B. Lin, G. Gibson, S.-C. Tsay, K. Stamnes, and T. Wong, 2000: δ-Fit: A fast and accurate treatment of particle scattering phase functions with weighted singular-value decomposition least-squares fitting. *J. Quant. Spectrosc. Radiat. Transfer*, **65**, 681–690, https://doi.org/10.1016/S0022-4073(99)00147-8.

Huang, Y., S. T. Siems, M. J. Manton, and G. Thompson, 2014: An evaluation of WRF simulations of clouds over the Southern Ocean with A-Train observations. *Mon. Wea. Rev.*, **142**, 647–667, https://doi.org/10.1175/MWR-D-13-00128.1.

Hudak, D., H. Barker, P. Rodriguez, and D. Donovan, 2006: The Canadian CloudSat validation project. *Fourth European Conf. on Radar in Hydrology and Meteorology*, Barcelona, Spain, ERAD, 609–612.

Huffman, G. J., R. F. Adler, D. T. Bolvin, and G. Gu, 2009: Improving the global precipitation record: GPCP version 2.1. *Geophys. Res. Lett.*, **36**, L17808, https://doi.org/10.1029/2009GL040000.

Iwabuchi, H., and P. Yang, 2011: Temperature dependence of ice optical constants: Implications for simulating the single-scattering properties of cold ice clouds. *J. Quant. Spectrosc. Radiat. Transfer*, **112**, 2520–2525, https://doi.org/10.1016/j.jqsrt.2011.06.017.

Jiang, J. H., and Coauthors, 2012: Evaluation of cloud and water vapor simulations in CMIP5 climate models using NASA "A-Train" satellite observations. *J. Geophys. Res.*, **117**, D14105, https://doi.org/10.1029/2011JD017237.

Johnson, B. R., 1988: Invariant imbedding T matrix approach to electromagnetic scattering. *Appl. Opt.*, **27**, 4861–4873, https://doi.org/10.1364/AO.27.004861.

Johnson, B. T., G. W. Petty, and G. Skofronick-Jackson, 2012: Microwave properties of ice-phase hydrometeors for radar and radiometers: Sensitivity to model assumptions. *J. Appl. Meteor. Climatol.*, **51**, 2152–2171, https://doi.org/10.1175/JAMC-D-11-0138.1.

——, W. S. Olson, and G. Skofronick-Jackson, 2016: The microwave properties of simulated melting precipitation particles: Sensitivity to initial melting. *Atmos. Meas. Tech.*, **9**, 9–21, https://doi.org/10.5194/amt-9-9-2016.

Kazumori, M., and S. J. English, 2015: Use of the ocean surface wind direction signal in microwave radiance assimilation. *Quart. J. Roy. Meteor. Soc.*, **141**, 1354–1375, https://doi.org/10.1002/qj.2445.

Kim, M.-J., 2006: Single scattering parameters of randomly oriented snow particles at microwave frequencies. *J. Geophys. Res.*, **111**, D14201, https://doi.org/10.1029/2005JD006892.

——, M. S. Kulie, C. O'Dell, and R. Bennartz, 2007: Scattering of ice particles at microwave frequencies: A physically based parameterization. *J. Appl. Meteor. Climatol.*, **46**, 615–633, https://doi.org/10.1175/JAM2483.1.

Kneifel, S., M. S. Kulie, and R. Bennartz, 2011: A triple-frequency approach to retrieve microphysical snowfall parameters. *J. Geophys. Res.*, **116**, D11203, https://doi.org/10.1029/2010JD015430.

Kobayashi, T., 2007: Significant differences in the cloud droplet effective radius between nonprecipitating and precipitating clouds. *Geophys. Res. Lett.*, **34**, L15811, https://doi.org/10.1029/2007GL029606.

Kulie, M. S., and R. Bennartz, 2009: Utilizing spaceborne radars to retrieve dry snowfall. *J. Appl. Meteor. Climatol.*, **48**, 2564–2580, https://doi.org/10.1175/2009JAMC2193.1.

——, ——, T. J. Greenwald, Y. Chen, and F. Weng, 2010: Uncertainties in microwave properties of frozen precipitation: Implications for remote sensing and data assimilation. *J. Atmos. Sci.*, **67**, 3471–3487, https://doi.org/10.1175/2010JAS3520.1.

——, L. Milani, N. B. Wood, and T. S. L'Ecuyer, 2020: Global snowfall detection and measurement. *Satellite Precipitation Measurement*, V. Levizzani et al., Eds., Springer, 699–716.

Kummerow, C., and J. A. Weinman, 1988: Determining microwave brightness temperatures from precipitating horizontally finite and vertically structured clouds. *J. Geophys. Res.*, **93**, 3720–3728, https://doi.org/10.1029/JD093iD04p03720.

——, W. S. Olson, and L. Giglio, 1996: A simplified scheme for obtaining precipitation and vertical hydrometeor profiles from passive microwave sensors. *IEEE Trans. Geosci. Remote Sens.*, **34**, 1213–1232, https://doi.org/10.1109/36.536538.

——, W. Barnes, T. Kozu, J. Shiue, and J. Simpson, 1998: The Tropical Rainfall Measuring Mission (TRMM) sensor package. *J. Atmos. Oceanic Technol.*, **15**, 809–817, https://doi.org/10.1175/1520-0426(1998)015<0809:TTRMMT>2.0.CO;2.

——, and Coauthors, 2000: The status of the Tropical Rainfall Measuring Mission (TRMM) after two years in orbit. *J. Appl. Meteor. Climatol.*, **39**, 1965–1982, https://doi.org/10.1175/1520-0450(2001)040<1965:TSOTTR>2.0.CO;2.

——, and Coauthors, 2001: The evolution of the Goddard Profiling Algorithm (GPROF) for rainfall estimation from passive microwave sensors. *J. Appl. Meteor.*, **40**, 1801–1820, https://doi.org/10.1175/1520-0450(2001)040<1801:TEOTGP>2.0.CO;2.

Kuo, K.-S., and Coauthors, 2016: The microwave radiative properties of falling snow derived from nonspherical ice particle models. Part I: An extensive database of simulated pristine crystals and aggregate particles, and their scattering properties. *J. Appl. Meteor. Climatol.*, **55**, 691–708, https://doi.org/10.1175/JAMC-D-15-0130.1.

Lebsock, M. D., and T. S. L'Ecuyer, 2011: The retrieval of warm rain from CloudSat. *J. Geophys. Res.*, **116**, D20209, https://doi.org/10.1029/2011JD016076.

L'Ecuyer, T. S., and G. L. Stephens, 2002: An estimation-based precipitation retrieval algorithm for attenuating radars. *J. Appl. Meteor. Climatol.*, **41**, 272–285, https://doi.org/10.1175/1520-0450(2002)041<0272:AEBPRA>2.0.CO;2.

Leinonen, J., S. Kneifel, D. Moisseev, J. Tyynelä, S. Tanelli, and T. Nousiainen, 2012: Evidence of nonspheroidal behavior in millimeter-wavelength radar observations of snowfall. *J. Geophys. Res.*, **117**, D18205, https://doi.org/10.1029/2012JD017680.

Liu, C., P. Yang, P. Minnis, N. Loeb, S. Kato, A. Heymsfield, and C. Schmitt, 2014: A two-habit model for the microphysical and optical properties of ice clouds. *Atmos. Chem. Phys.*, **14**, 13 719–13 737, https://doi.org/10.5194/acp-14-13719-2014.

Liu, G., 2004: Approximation of single scattering properties of ice and snow particles for high microwave frequencies. *J. Atmos. Sci.*, **61**, 2441–2456, https://doi.org/10.1175/1520-0469(2004)061<2441:AOSSPO>2.0.CO;2.

——, 2008a: A database of microwave single-scattering properties for nonspherical ice particles. *Bull. Amer. Meteor. Soc.*, **89**, 1563–1570, https://doi.org/10.1175/2008BAMS2486.1.

——, 2008b: Deriving snow cloud characteristics from CloudSat observations. *J. Geophys. Res.*, **113**, D00A09, https://doi.org/10.1029/2007JD009766.

——, and E.-K. Seo, 2013: Detecting snowfall over land by satellite high-frequency microwave observations: The lack of scattering signature and a statistical approach. *J. Geophys. Res. Atmos.*, **118**, 1376–1387, https://doi.org/10.1002/jgrd.50172.

Liu, Q., and F. Weng, 2006: Advanced doubling–adding method for radiative transfer in planetary atmospheres. *J. Atmos. Sci.*, **63**, 3459–3465, https://doi.org/10.1175/JAS3808.1.

——, ——, and S. J. English, 2011: An improved fast microwave water emissivity model. *IEEE Trans. Geosci. Remote Sens.*, **49**, 1238–1250, https://doi.org/10.1109/TGRS.2010.2064779.

Loeb, N. G., and Coauthors, 2018: Impact of ice cloud microphysics on satellite cloud retrievals and broadband flux radiative transfer model calculations. *J. Climate*, **31**, 1851–1864, https://doi.org/10.1175/JCLI-D-17-0426.1.

Lu, Q., and Coauthors, 2020: Monitoring the performance of the Fengyun satellite instruments using radiative transfer models and NWP fields. *J. Quant. Spectrosc. Radiat. Transfer*, **255**, 107239, https://doi.org/10.1016/j.jqsrt.2020.107239.

Lu, Y., Z. Jiang, K. Aydin, J. Verlinde, E. E. Clothiaux, and G. Botta, 2016: A polarimetric scattering database for nonspherical ice particles at microwave wavelengths. *Atmos. Meas. Tech.*, **9**, 5119–5134, https://doi.org/10.5194/amt-9-5119-2016.

Madden, R. A., and P. R. Julian, 1971: Detection of a 40–50 day oscillation in the zonal wind in the tropical Pacific. *J. Atmos. Sci.*, **28**, 702–708, https://doi.org/10.1175/1520-0469(1971)028<0702:DOADOI>2.0.CO;2.

——, and ——, 1972: Description of global-scale circulation cells in the tropics with a 40–50 day period. *J. Atmos. Sci.*, **29**, 1109–1123, https://doi.org/10.1175/1520-0469(1972)029<1109:DOGSCC>2.0.CO;2.

Marchand, R., G. G. Mace, T. Ackerman, and G. Stephens, 2008: Hydrometeor detection using *CloudSat*—An Earth-orbiting 94-GHz cloud radar. *J. Atmos. Oceanic Technol.*, **25**, 519–533, https://doi.org/10.1175/2007JTECHA1006.1.

Masunaga, H., M. Satoh, and H. Miura, 2008: A joint satellite and global cloud-resolving model analysis of a Madden–Julian oscillation event: Model diagnosis. *J. Geophys. Res.*, **113**, D17210, https://doi.org/10.1029/2008JD009986.

——, and Coauthors, 2010: Satellite data simulator unit: A multisensor, multispectral satellite simulator package. *Bull. Amer. Meteor. Soc.*, **91**, 1625–1632, https://doi.org/10.1175/2010BAMS2809.1.

Matrosov, S. Y., 2007: Modeling backscatter properties of snowfall at millimeter wavelengths. *J. Atmos. Sci.*, **64**, 1727–1736, https://doi.org/10.1175/JAS3904.1.

——, 2019: Comparative evaluation of snowfall retrievals from the *CloudSat* W-band radar using ground-based weather radars. *J. Atmos. Oceanic Technol.*, **36**, 101–111, https://doi.org/10.1175/JTECH-D-18-0069.1.

——, and A. Battaglia, 2009: Influence of multiple scattering on *CloudSat* measurements in snow: A model study. *Geophys. Res. Lett.*, **36**, L12806, https://doi.org/10.1029/2009GL038704.

——, M. D. Shupe, and I. V. Djalalova, 2008: Snowfall retrievals using millimeter-wavelength cloud radars. *J. Appl. Meteor. Climatol.*, **47**, 769–777, https://doi.org/10.1175/2007JAMC1768.1.

Matsui, T., X. Zeng, W.-K. Tao, H. Masunaga, W. S. Olson, and S. Lang, 2009: Evaluation of long-term cloud-resolving model simulations using satellite radiance observations and multifrequency satellite simulators. *J. Atmos. Oceanic Technol.*, **26**, 1261–1274, https://doi.org/10.1175/2008JTECHA1168.1.

——, and Coauthors, 2013: GPM satellite simulator over ground validation sites. *Bull. Amer. Meteor. Soc.*, **94**, 1653–1660, https://doi.org/10.1175/BAMS-D-12-00160.1.

——, and Coauthors, 2014: Introducing multisensor satellite radiance-based evaluation for regional Earth system modeling. *J. Geophys. Res. Atmos.*, **119**, 8450–8475, https://doi.org/10.1002/2013JD021424.

Mitrescu, C., T. L'Ecuyer, J. Haynes, S. Miller, and J. Turk, 2010: *CloudSat* precipitation profiling algorithm—Model description. *J. Appl. Meteor. Climatol.*, **49**, 991–1003, https://doi.org/10.1175/2009JAMC2181.1.

Mroz, K., M. Montopoli, A. Battaglia, G. Panegrossi, P. Kirstetter, and L. Baldini, 2021: Cross validation of active and passive microwave snowfall products over the continental United States. *J. Hydrometeor.*, **22**, 1297–1315, https://doi.org/10.1175/JHM-D-20-0222.1.

Norin, L., A. Devasthale, T. L'Ecuyer, N. B. Wood, and M. Smalley, 2015: Intercomparison of snowfall estimates derived from the CloudSat cloud profiling radar and the ground-based weather radar network over Sweden. *Atmos. Meas. Tech.*, **8**, 5009–5021, https://doi.org/10.5194/amt-8-5009-2015.

Nowell, H., G. Liu, and R. Honeyager, 2013: Modeling the microwave single-scattering properties of aggregate snowflakes. *J. Geophys. Res. Atmos.*, **118**, 7873–7885, https://doi.org/10.1002/jgrd.50620.

Olson, W. S., and Coauthors, 2016: The microwave radiative properties of falling snow derived from nonspherical ice particle models. Part II: Initial testing using radar, radiometer and in situ observations. *J. Appl. Meteor. Climatol.*, **55**, 709–722, https://doi.org/10.1175/JAMC-D-15-0131.1.

Ori, D., L. von Terzi, M. Karrer, and S. Kneifel, 2021: snowscatt 1.0: Consistent model of microphysical and scattering properties of rimed and unrimed snowflakes based on the self-similar Rayleigh–Gans approximation. *Geosci. Model Dev.*, **14**, 1511–1531, https://doi.org/10.5194/gmd-14-1511-2021.

Otkin, J. A., T. J. Greenwald, J. Sieglaff, and H.-L. Huang, 2009: Validation of a large-scale simulated brightness temperature dataset using SEVIRI satellite observations. *J. Appl. Meteor. Climatol.*, **48**, 1613–1626, https://doi.org/10.1175/2009JAMC2142.1.

Petty, G. W., and W. Huang, 2010: Microwave backscatter and extinction by soft ice spheres and complex snow aggregates. *J. Atmos. Sci.*, **67**, 769–787, https://doi.org/10.1175/2009JAS3146.1.

——, and R. Bennartz, 2017: Field-of-view characteristics and resolution matching for the Global Precipitation Measurement (GPM) Microwave Imager (GMI). *Atmos. Meas. Tech.*, **10**, 745–758, https://doi.org/10.5194/amt-10-745-2017.

Platnick, S., and Coauthors, 2017: The MODIS cloud optical and microphysical products: Collection 6 updates and examples from *Terra* and *Aqua*. *IEEE Trans. Geosci. Remote Sens.*, **55**, 502–525, https://doi.org/10.1109/TGRS.2016.2610522.

Pruppacher, H. R., and J. D. Klett, 2010: *Microphysics of Clouds and Precipitation*. 2nd ed. Springer, 954 pp.

Qu, Z., and Coauthors, 2018: Evaluation of a high-resolution numerical weather prediction model's simulated clouds using observations from *CloudSat*, *GOES-13* and in situ aircraft. *Quart. J. Roy. Meteor. Soc.*, **144**, 1681–1694, https://doi.org/10.1002/qj.3318.

Rapp, A. D., 2016: Observational evidence linking precipitation and mesoscale cloud fraction in the southeast Pacific. *Geophys. Res. Lett.*, **43**, 7267–7273, https://doi.org/10.1002/2016GL069906.

——, M. Lebsock, and T. L'Ecuyer, 2013: Low cloud precipitation climatology in the southeastern Pacific marine stratocumulus region using *CloudSat*. *Environ. Res. Lett.*, **8**, 014027, https://doi.org/10.1088/1748-9326/8/1/014027.

Ren, T., D. Li, J. Muller, and P. Yang, 2021: Sensitivity of radiative flux simulations to ice cloud parameterization over the equatorial western Pacific Ocean region. *J. Atmos. Sci.*, **78**, 2549–2571, https://doi.org/10.1175/JAS-D-21-0017.1.

Saunders, R., and Coauthors, 2018: An update on the RTTOV fast radiative transfer model (currently at version 12). *Geosci. Model Dev.*, **11**, 2717–2737, https://doi.org/10.5194/gmd-11-2717-2018.

Sieron, S. B., E. E. Clothiaux, F. Zhang, Y. Lu, and J. A. Otkin, 2017: Comparison of using distribution-specific versus effective radius methods for hydrometeor single-scattering properties for all-sky microwave satellite radiance simulations with different microphysics parameterization schemes. *J. Geophys. Res. Atmos.*, **122**, 7027–7046, https://doi.org/10.1002/2017JD026494.

——, F. Zhang, E. E. Clothiaux, L. N. Zhang, and Y. Lu, 2018: Representing precipitation ice species with both spherical and nonspherical particles for radiative transfer modeling of microphysics-consistent cloud microwave scattering properties.

J. Adv. Model. Earth Syst., **10**, 1011–1028, https://doi.org/10.1002/2017MS001226.

Skofronick-Jackson, G., and B. T. Johnson, 2011: Surface and atmospheric contributions to passive microwave brightness temperatures for falling snow events. *J. Geophys. Res.*, **116**, D02213, https://doi.org/10.1029/2010JD014438.

Souverijns, N., and Coauthors, 2018: Evaluation of the *CloudSat* surface snowfall product over Antarctica using ground-based precipitation radars. *Cryosphere*, **12**, 3775–3789, https://doi.org/10.5194/tc-12-3775-2018.

Stegmann, P. G., G. Tang, P. Yang, and B. T. Johnson, 2018: A stochastic model for density-dependent microwave snow- and graupel scattering coefficients of the NOAA JCSDA community radiative transfer model. *J. Quant. Spectrosc. Radiat. Transfer*, **211**, 9–24, https://doi.org/10.1016/j.jqsrt.2018.02.026.

Stephens, G. L., and Coauthors, 2002: The *CloudSat* mission and the A-Train: A new dimension of space-based observations of clouds and precipitation. *Bull. Amer. Meteor. Soc.*, **83**, 1771–1790, https://doi.org/10.1175/BAMS-83-12-1771.

Su, H., and Coauthors, 2013: Diagnosis of regime-dependent cloud simulation errors in CMIP5 models using "A-Train" satellite observations and reanalysis data. *J. Geophys. Res. Atmos.*, **118**, 2762–2780, https://doi.org/10.1029/2012JD018575.

Sun, L., A. D. Rapp, T. S. L'Ecuyer, A. S. Daloz, and E. Nelson, 2022: Environmental response in coupled energy and water cloud impact parameters derived from A-Train satellite, ERA-Interim, and MERRA-2. *J. Appl. Meteor. Climatol.*, **61**, 261–276, https://doi.org/10.1175/JAMC-D-21-0078.1.

Tanelli, S., and Coauthors, 2008: *CloudSat*'s cloud profiling radar after two years in orbit: Performance, calibration, and processing. *IEEE Trans. Geosci. Remote Sens.*, **46**, 3560–3573, https://doi.org/10.1109/TGRS.2008.2002030.

Tang, G., P. Yang, P. G. Stegmann, R. L. Panetta, L. Tsang, and B. Johnson, 2017: Effect of particle shape, density, and inhomogeneity on the microwave optical properties of graupel and hailstones. *IEEE Trans. Geosci. Remote Sens.*, **55**, 6366–6378, https://doi.org/10.1109/TGRS.2017.2726994.

Thompson, G., and T. Eidhammer, 2014: A study of aerosol impacts on clouds and precipitation development in a large winter cyclone. *J. Atmos. Sci.*, **71**, 3636–3658, https://doi.org/10.1175/JAS-D-13-0305.1.

——, R. M. Rasmussen, and K. Manning, 2004: Explicit forecasts of winter precipitation using an improved bulk microphysics scheme. Part I: Description and sensitivity analysis. *Mon. Wea. Rev.*, **132**, 519–542, https://doi.org/10.1175/1520-0493(2004)132<0519:EFOWPU>2.0.CO;2.

——, P. R. Field, R. M. Rasmussen, and W. D. Hall, 2008: Explicit forecasts of winter precipitation using an improved bulk microphysics scheme. Part II: Implementation of a new snow parameterization. *Mon. Wea. Rev.*, **136**, 5095–5115, https://doi.org/10.1175/2008MWR2387.1.

——, M. Tewari, K. Ikeda, S. Tessendorf, C. Weeks, J. Otkin, and F. Kong, 2016: Explicitly-coupled cloud physics and radiation parameterizations and subsequent evaluation in WRF high-resolution convective forecasts. *Atmos. Res.*, **168**, 92–104, https://doi.org/10.1016/j.atmosres.2015.09.005.

Turk, F. J., and Coauthors, 2021: Applications of a *CloudSat*–TRMM and *CloudSat*–GPM satellite coincidence dataset. *Remote Sens.*, **13**, 2264, https://doi.org/10.3390/rs13122264.

Tyynelä, J., and A. von Lerber, 2019: Validation of microphysical snow models using in situ, multifrequency, and dual-polarization radar measurements in Finland. *J. Geophys. Res. Atmos.*, **124**, 13 273–13 290, https://doi.org/10.1029/2019JD030721.

——, J. Leinonen, D. Moisseev, and T. Nousiainen, 2011: Radar backscattering from snowflakes: Comparison of fractal, aggregate, and soft spheroid models. *J. Atmos. Oceanic Technol.*, **28**, 1365–1372, https://doi.org/10.1175/JTECH-D-11-00004.1.

van de Hulst, H. C., 1957: *Light Scattering by Small Particles*. Dover Publications, Inc., 470 pp.

——, 1974: The spherical albedo of a planet covered with a homogeneous cloud layer. *Astron. Astrophys.*, **35**, 209–214.

Vignesh, P. P., J. H. Jiang, P. Kishore, H. Su, T. Smay, N. Brighton, and I. Velicogna, 2020: Assessment of CMIP6 cloud fraction and comparison with satellite observations. *Earth Space Sci.*, **7**, e2019EA000975, https://doi.org/10.1029/2019EA000975.

Wang, P.-K., 1982: Mathematical description of the shape of conical hydrometeors. *J. Atmos. Sci.*, **39**, 2615–2622, https://doi.org/10.1175/1520-0469(1982)039<2615:MDOTSO>2.0.CO;2.

Wang, Y., G. Liu, E.-K. Seo, and Y. Fu, 2013: Liquid water in snowing clouds: Implications for satellite remote sensing of snowfall. *Atmos. Res.*, **131**, 60–72, https://doi.org/10.1016/j.atmosres.2012.06.008.

Warren S. G., and R. E. Brandt, 2008: Optical constants of ice from the ultraviolet to the microwave: A revised compilation. *J. Geophys. Res.*, **113**, D14220, https://doi.org/10.1029/2007JD009744.

Wilheit, T. T., A. Chang, M. S. V. Rao, E. B. Rodgers, and J. S. Theon, 1977: A satellite technique for quantitatively mapping rainfall rates over the oceans. *J. Appl. Meteor. Climatol.*, **16**, 551–560, https://doi.org/10.1175/1520-0450(1977)016<0551:ASTFQM>2.0.CO;2.

Wood, N. B., and T. S. L'Ecuyer, 2021: What millimeter-wavelength radar reflectivity reveals about snowfall: An information-centric analysis. *Atmos. Meas. Tech.*, **14**, 869–888, https://doi.org/10.5194/amt-14-869-2021.

——, ——, F. L. Bliven, and G. L. Stephens, 2013: Characterization of video disdrometer uncertainties and impacts on estimates of snowfall rate and radar reflectivity. *Atmos. Meas. Tech.*, **6**, 3635–3648, https://doi.org/10.5194/amt-6-3635-2013.

——, ——, A. J. Heymsfield, G. L. Stephens, D. R. Hudak, and P. Rodriguez, 2014: Estimating snow microphysical properties using collocated multisensor observations. *J. Geophys. Res. Atmos.*, **119**, 8941–8961, https://doi.org/10.1002/2013JD021303.

——, ——, ——, and ——, 2015: Microphysical constraints on millimeter-wavelength scattering properties of snow particles. *J. Appl. Meteor. Climatol.*, **54**, 909–931, https://doi.org/10.1175/JAMC-D-14-0137.1.

Wyser, K., and P. Yang, 1998: Average ice crystal size and bulk short-wave single-scattering properties of cirrus clouds. *Atmos. Res.*, **49**, 315–335, https://doi.org/10.1016/S0169-8095(98)00083-0.

Yang, P., and K. N. Liou, 1996: Geometric-optics–integral-equation method for light scattering by nonspherical ice crystals. *Appl. Opt.*, **35**, 6568–6584, https://doi.org/10.1364/AO.35.006568.

——, G. W. Kattawar, K.-N. Liou, and J. Q. Lu, 2004: Comparison of Cartesian grid configurations for application of the finite-difference time-domain method to electromagnetic scattering by dielectric particles. *Appl. Opt.*, **43**, 4611–4624, https://doi.org/10.1364/AO.43.004611.

——, L. Bi, B. A. Baum, K.-N. Liou, G. W. Kattawar, M. I. Mishchenko, and B. Cole, 2013: Spectrally consistent scattering, absorption, and polarization properties of atmospheric ice crystals at wavelengths from 0.2 to 100 μm. *J. Atmos. Sci.*, **70**, 330–347, https://doi.org/10.1175/JAS-D-12-039.1.

——, J. Ding, R. L. Panetta, K.-N. Liou, G. Kattawar, and M. I. Mishchenko, 2019: On the convergence of numerical computations for both exact and approximate solutions for

electromagnetic scattering by nonspherical dielectric particles. *Prog. Electromagn. Res.*, **164**, 27–61, https://doi.org/10.2528/PIER18112810.

Yi, B., P. Yang, Q. Liu, P. van Delst, S.-A. Boukabara, and F. Weng, 2016: Improvements on the ice cloud modeling capabilities of the community radiative transfer model. *J. Geophys. Res. Atmos.*, **121**, 13 577–13 590, https://doi.org/10.1002/2016JD025207.

Yin, M., and G. Liu, 2017: Developing an a priori database for passive microwave snow water retrievals over ocean. *J. Geophys. Res. Atmos.*, **122**, 12 960–12 981, https://doi.org/10.1002/2017JD027636.

——, and ——, 2019: Assessment of GPM high-frequency microwave measurements with radiative transfer simulation under snowfall conditions. *Quart. J. Roy. Meteor. Soc.*, **145**, 1603–1616, https://doi.org/10.1002/qj.3515.

Zhang, J., and Coauthors, 2016: Multi-Radar Multi-Sensor (MRMS) quantitative precipitation estimation: Initial operating capabilities. *Bull. Amer. Meteor. Soc.*, **97**, 621–638, https://doi.org/10.1175/BAMS-D-14-00174.1.

Zhang, Y., and Coauthors, 2021: Ensemble-based assimilation of satellite all-sky microwave radiances improves intensity and rainfall predictions for Hurricane Harvey (2017). *Geophys. Res. Lett.*, **48**, e2021GL096410, https://doi.org/10.1029/2021GL096410.

Zhou, Y. P., and Coauthors, 2007: Use of high-resolution satellite observations to evaluate cloud and precipitation statistics from cloud-resolving model simulations. Part I: South China Sea Monsoon Experiment. *J. Atmos. Sci.*, **64**, 4309–4329, https://doi.org/10.1175/2007JAS2281.1.

Zhu, Y., and Coauthors, 2016: All-sky microwave radiance assimilation in NCEP's GSI analysis system. *Mon. Wea. Rev.*, **144**, 4709–4735, https://doi.org/10.1175/MWR-D-15-0445.1.